Chapter 5

Design of Time-Dependent Non-Reflecting Boundary Conditions: The Three-Dimensional Case

As discussed in the introduction to this thesis, numerical methods for solution of the exterior structural acoustics problem may be characterized in terms of the local (differential) or non-local (integral) spatial and temporal operators appearing in the formulation, see Table 5.1. An example of a nonlocal representation for the infinite fluid is the direct time-integration of Kirchhoff's retarded potential boundary integral, see e.g. MANSUR AND BREBBIA [1984], NEILSON et al. [1981]. This method leads to unsymmetric and dense matrices and, more importantly, can be extremely memory intensive, typically requiring storage of a large pool of historical data during the solution process. The direct convolution of the DtN map GIVOLI [1988] is also nonlocal in space and time, requiring convolution over all past time up to the current solution.

Because of the limitations and difficulties noted above there is a need for the development of local in time non-reflecting (absorbing) boundary conditions which eliminate or minimize reflection of outgoing waves and that also preserve the data structure of the finite element method. If accurate non-reflecting boundary conditions are used, then the fluid truncation boundary can be moved closer to the structure.

Table 5.1: Computational methods for representation of unbounded media: Summary of characteristics in terms of applicability (Y) or non-applicability (N) to transient and time-harmonic analysis, and in terms of the local (Y) or nonlocal (N) character of the spatial and temporal dependence.

Methods based on exact representations	Harmonic Analysis	Transient Analysis	Local in Space	Local in Time
Boundary element method	Y	Y	N	N
Dirichlet-to-Neumann map	Y	Y	N	N
Methods based on approximate representations	**Harmonic Analysis**	**Transient Analysis**	**Local in Space**	**Local in Time**
Plane-wave damper	Y	Y	Y	Y
DAA	Y	Y	N	Y
Infinite elements	Y	N	Y	–
Higher-order NRBC	Y	Y	Y	Y

In this case the finite element model will be able to use fewer fluid elements and considerable cost savings will result. Approximate non-reflecting boundary conditions that are local in time (i.e. differential operators in time) have been proposed by several authors. As discussed earlier in Chapter 2, the simplest possible boundary condition takes the form of the Sommerfeld radiation condition at infinity (2.24), repeated here as,

$$\frac{\partial \phi}{\partial n} = -\mathbb{S}_0 \phi, \qquad \text{where} \quad \mathbb{S}_0 := \frac{1}{c}\frac{\partial}{\partial t} \tag{5.1}$$

As noted this operator is sometimes referred to as the 'plane-wave' (PW) damper. The term damper is used to indicate that the operator takes the form of a local 'dashpot' applied to the fluid truncation boundary which absorbs energy leaving the system. The PW-damper was first used by Mindlin and Bleich [1953] to study the response of an elastic shell to a transient shock wave, and later in the context of the semidiscrete finite element method by Zienkewicz [1969,1977]. It can be shown that this simple boundary condition is exact in one-dimension, however in multi-dimensions the performance is known to deteriorate significantly as the position of the artificial boundary approaches the source of radiation, especially in the low-frequency (long wavelength) limit, where the virtual mass (or added mass) approximation of incompressibility is more appropriate, Chertock [1970] .

The doubly asymptotic approximation (DAA) on the other hand, is asymptotically exact in the high-frequency and low-frequency limits and through a consistent matching approximates the exact impedance throughout the intermediate frequency range, GEERS [1971,1978]. The DAA operator essentially matches the local in time PW-damper in the high-frequency limit to the non-local boundary integral representation of the Laplacian operator in the low-frequency limit. A family of DAA's has been derived by the method of matched asymptotic expansions in FELIPPA [1980], and NICOLAS [1989]; though successful implementation to large-scale transient computations involving complex structures seems to be limited to the first member of that family only NEILSON [1981], FELIPPA [1984] and RUZICKA [1989]. As the low-order DAA has difficulty accurately capturing the response over a large range of middle frequencies for complex systems, there is strong motivation to obtain improved non-reflecting boundary conditions that are local in time, and yield highly accurate solutions over a wide range of important frequencies.

High-order accurate non-reflecting boundary conditions that are local in time have been proposed by several authors; complete surveys can be found in GIVOLI [1991] and ABBOUD [1990]. Here we mention the well-known sequence of boundary conditions derived by ENGQUIST AND MAJDA [1977,1979]. In this approach operators of increasing order are obtained using rational approximations to a pseudo-differential operator in the frequency domain. Time-dependent boundary conditions are obtained through an inverse Fourier transform. BAYLISS AND TURKEL [1980,1982], introduced an alternative sequence of local boundary operators derived from a power series (multipole) expansion of the exact solution in negative powers of the radial distance from the source.

In this chapter, new time-dependent non-reflecting boundary conditions are developed for the wave equation in three-dimensions. Two alternative sequences of radiation boundary operators are derived; the first involves both time and spatial derivatives (local in time and local in space version), and the second involves time derivatives yet retains a spatial integral (local in time and nonlocal in space version). The local in time and local in space version starts from the exact localization of the nonlocal impedance relation (DtN map) in the frequency domain (GIVOLI AND KELLER [1990], HARARI [1991a]). Time-dependent boundary conditions are then obtained through the application of an inverse Fourier transform, see Figure 5.1 for

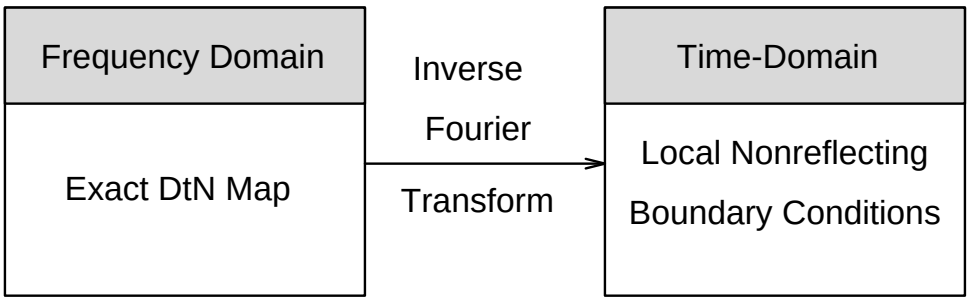

Figure 5.1: Schematic for the development of non-reflecting boundary conditions. Starting in the frequency domain with the exact Dirichlet-to-Neumann (DtN) impedance relation, an inverse Fourier transform is used to obtain the exact local time-dependent counterpart.

a schematic of the procedure. Since these time-dependent boundary conditions follow directly from the exact impedance expressed through the DtN map, the first N operators in this new sequence exactly represent the first N spherical wave harmonics for outgoing waves. In contrast to nonlocal boundary conditions, the proposed local boundary conditions preserve the data structure of the finite element method and require only local storage of historical data during the solution process. In addition, we show that an inverse Fourier transform exists for the frequency dependent Dirichlet-to-Neumann (DtN) map Keller and Givoli [1989], allowing for boundary conditions that are nonlocal in space yet retain the important property of locality in time. The non-reflecting boundary conditions developed in this Chapter are implemented as natural boundary conditions in the time-discontinuous GLS formulation, i.e. they are weakly enforced in both space and time.

5.1 Dirichlet-to-Neumann Map in the Frequency Domain

In order to obtain a sequence of time-dependent non-reflecting boundary conditions which are exact for the first N spherical wave harmonics on the truncation boundary Γ_∞, we start with the Dirichlet-to-Neumann (DtN) map in the frequency domain. The DtN map represents the exact impedance for the infinite acoustic fluid restricted

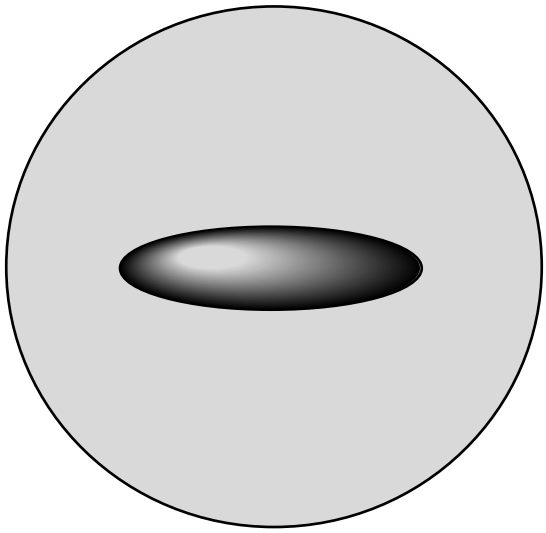

Figure 5.2: Illustration of a finite computational domain enclosed by a spherical artificial boundary of radius R.

to an artificial boundary of separable geometry, e.g. a sphere of radius $r = R$ in $\mathbb{R}^3$, see Figure 5.2. Assuming harmonic time dependence $e^{-i\omega t}$, with frequency $\omega > 0$, the exact non-local Dirichlet-to-Neumann (DtN) boundary condition in the frequency domain can be expressed in terms of an infinite series of spherical wave harmonics, see e.g. KELLER AND GIVOLI [1989]:

$$\boxed{\frac{\partial \phi}{\partial n}(R,\theta,\varphi) = \sum_{n=0}^{\infty} z_n \int_{\Gamma_\infty} s_n(\theta,\varphi,\theta',\varphi')\ \phi(R,\theta',\varphi')\ d\Gamma'} \tag{5.2}$$

where the DtN kernels $s_n,\ n = 0, 1, 2, \cdots$ are given by,

$$s_n = \sum_{j=0}^{n} {}'\alpha_{nj} P_n^j(\cos\varphi) P_n^j(\cos\varphi') \cos j(\theta - \theta') \tag{5.3}$$

$$\alpha_{nj} = \frac{(2n+1)(n-j)!}{2\pi R^2 (n+j)!} \tag{5.4}$$

with impedance coefficients,

$$z_n(kR) = \frac{k h_n'(kR)}{h_n(kR)} \tag{5.5}$$

In the above, $k = \omega/c$ is the acoustic wavenumber, $0 \leq \theta < 2\pi$ is the circumferential angle and $0 \leq \varphi < \pi$ is the polar angle for a spherical truncation boundary of radius $r = R$. The differential surface area is $d\Gamma = R^2 \sin\varphi d\theta d\varphi$, P_n^j are associated Legendre functions of the first kind, and h_n are spherical Hankel function of the first kind of order n. The prime on h_n indicates differentiation with respect to its argument, and the prime after the sum indicates that a factor of $1/2$ multiplies the term with $j = 0$. The boundary condition (5.2) can be written in operator form as,

$$\frac{\partial \phi}{\partial n} = -\mathbb{S}\ \phi \qquad \text{on} \quad \Gamma_\infty \tag{5.6}$$

relating Dirichlet data, ϕ, to Neumann data, $\partial\phi/\partial n$, through the linear mapping $\mathbb{S} : \phi \mapsto \partial\phi/\partial n$. This operator represents the exact impedance of the exterior domain restricted to Γ_∞. The DtN map $\mathbb{S}$, is an integral operator resulting in a nonlocal boundary condition coupling all points on the artificial boundary Γ_∞. When implemented in a finite element method, the matrices emanating from the discretization of this nonlocal boundary condition are fully populated and dense.

Direct time-convolution of the DtN map

The direct time convolution of the DtN map $\mathbb{S}$, is discussed in Givoli [1988] and can be expressed in operator form as,

$$\frac{\partial \phi}{\partial n}(\boldsymbol{x}\ ,\ t) = \int_0^t \int_{\Gamma_\infty} s(\boldsymbol{x}\ ,\ \boldsymbol{x}'\ ,\ t-\tau)\ \phi(\boldsymbol{x}'\ ,\ \tau)\ d\Gamma'\ d\tau \tag{5.7}$$

This equation denotes a functional of the values of $\phi(\boldsymbol{x}'\ ,\ \tau)$ for $\boldsymbol{x}'$ ranging over Γ_∞ and τ ranging from 0 to t, and expresses both spatial and temporal nonlocality. In other words, the convoluted DtN condition (5.7) indicates that at a given instant in time, the response at every point on the artificial boundary Γ_∞ is coupled with the time histories of all the other points on Γ_∞. Because this boundary condition involves a temporal integral over all past time, numerical solutions can be extremely memory-intensive, typically requiring storage of a large pool of historical data for typical solution times.

5.2 New Exact Time-Dependent Boundary Conditions

In order to circumvent the difficulty of having to solve a temporal convolution integral, two new sequences of time-dependent boundary conditions are derived in this section which replace the temporal integral with local temporal derivatives. This allows for the numerical solution to proceed in succession from one time step to the next with only local storage of data from the previous time step required. Two alternative sequences are derived; the first involves both time and spatial derivatives (local in time and local in space version), and the second involves time derivatives yet retains the spatial integral of the DtN map (local in time and nonlocal in space version).

To obtain exact time-dependent counterparts to the DtN map (5.2) which are local in time, use is made of the special property of spherical Hankel functions which can be represented as the finite series, (GRAFF [1975]):

$$h_n(kR) = h_0(kR)\left[(-i)^n \sum_{j=0}^{n} \frac{(n+j)!}{j!(n-j)} \left(\frac{-1}{2ikR}\right)^j\right], \quad n = 0, 1, 2, \cdots \tag{5.8}$$

Note that the zero order term $h_0 = \mathrm{e}^{ikR}/(ikR)$ can be taken outside the summation, and this series involves only inverse powers of the nondimensional wavenumber (ikR). As a result, simplified expressions can always be obtained for any order in terms of powers of $(ik)^j$, from which time-dependent counterparts are readily obtained from an inverse Fourier transform. In Chapter 6 it will be shown that a finite series representation for the non-half integer Hankel functions appearing in the two-dimensional case is not possible, and an alternative approach will then be necessary.

5.2.1 Local in time and local in space version

The goal of this section is to derive a sequence of non-reflecting boundary conditions that are local in both time and space, yet retain the desirable property of being exact for the first N outgoing spherical wave harmonics. We thus seek to replace the space-time convolution integral in (5.7) with local temporal and spatial derivatives.

Localization of the DtN map

In GIVOLI AND KELLER [1990], a spatially local counterpart to the non-local DtN map $\mathbb{S}$ defined in (5.2), is obtained in the frequency domain. These local boundary conditions inherit the property that they are exact for the first N wave harmonics. The operators were originally proposed for the two-dimensional case, and later extended to three-dimensions in HARARI [1991a]. The procedure for constructing these local boundary conditions in the frequency domain is summarized herein. We start by expressing the first N spherical wave harmonics in the truncated DtN map (5.2), in the alternative form,

$$\frac{\partial \phi}{\partial n}(R,\theta,\varphi) = \sum_{n=0}^{N-1} z_n \sum_{j=0}^{n} {}'P_n^j(\cos\varphi)(A_{nj}\cos j\theta + B_{nj}\sin j\theta) \tag{5.9}$$

where the coefficients A_{nj} and B_{nj} involve nonlocal spatial integrals over the artificial boundary. Expressing the solution restricted to Γ_∞, as a finite series of spherical surface harmonics,

$$\phi(R,\theta,\varphi) = \sum_{n=0}^{N-1} \sum_{j=0}^{n} {}'P_n^j(\cos\varphi)(A_{nj}\cos j\theta + B_{nj}\sin j\theta) \tag{5.10}$$

and differentiating with respect to the Laplace-Beltrami operator,

$$\boxed{\Delta_\Gamma \phi := \frac{1}{\sin\varphi}\frac{\partial}{\partial\varphi}\left(\sin\varphi\frac{\partial\phi}{\partial\varphi}\right) + \frac{1}{\sin^2\varphi}\frac{\partial^2\phi}{\partial\theta^2}} \tag{5.11}$$

to the mth power yields,

$$(-\Delta_\Gamma)^m \phi(R,\theta,\varphi) = \sum_{n=0}^{N-1} (n(n+1))^m \sum_{j=0}^{n} {}'P_n^j(\cos\varphi)(A_{nj}\cos j\theta + B_{nj}\sin j\theta) \tag{5.12}$$

Comparing (5.9) and (5.12) suggests expressing the impedance as the finite sum,

$$z_n = \sum_{m=0}^{N-1} (n(n+1))^m \beta_m, \qquad n = 0, 1, \cdots, N-1 \tag{5.13}$$

where β_m are obtained by solving this $N \times N$ linear algebraic system. Substituting this expansion into (5.9) and using (5.12), the nonlocal spatial integrals embedded in the coefficients A_{nj} and B_{nj} are replaced with local high-order tangential derivatives $(\Delta_\Gamma)^m$, and the following sequence of local boundary conditions are obtained:

$$\boxed{\frac{\partial \phi}{\partial n} \quad = \quad \sum_{m=0}^{N-1} \beta_m (-\Delta_\Gamma)^m \phi \qquad \text{on} \quad \Gamma_\infty} \tag{5.14}$$

Since the sequence defined in (5.14) follows directly from the truncated DtN map, the resulting radiation boundary operators are exact for waves consisting of the first N spherical harmonics. In this case, the nonlocal spatial integral has been replaced by a linear map expressed in terms of the differential operator $(\Delta_\Gamma)^m$. For further details see HARARI [1991a]. To obtain the exact time-dependent counterpart to the localized DtN non-reflecting boundary condition (5.14) defined in the frequency domain, use is made of the finite series expansion for spherical Hankel functions given in (5.8). Local in time counterparts are obtained through an inverse Fourier transform. The procedure is explicated by deriving the first three operators in the sequence.

First-order boundary condition

Consider the first operator in the sequence corresponding to $N = 1$; then (5.13) reduces to the simple result $z_0(kR) = \beta_0(kR)$, and the local DtN condition (5.14) specializes to,

$$\frac{\partial \phi}{\partial n} \quad = \quad \frac{k h_0'(kR)}{h_0(kR)} \phi \tag{5.15}$$

For clarity, set $h_n := h_n(kR)$, and use the relations,

$$h_0' = -h_1 \qquad \text{and} \qquad h_1 = \left(\frac{1}{kR} - i \right) h_0 \tag{5.16}$$

to obtain a simplified expression for (5.15):

$$\frac{\partial \phi}{\partial n} \quad = \quad \left(ik - \frac{1}{R} \right) \phi \tag{5.17}$$

The time-dependent counterpart to (5.17) is obtained by direct application of the inverse Fourier transform:

$$\phi(\boldsymbol{x}\,,\,t) := \frac{1}{\sqrt{2\pi}} \int_{-\infty}^{\infty} \phi(\boldsymbol{x}\,,\,\omega) e^{-i\omega t}\, d\omega \tag{5.18}$$

In effect, replacing every occurrence of the operator $-ik$ by $\frac{1}{c}\frac{\partial}{\partial t}$ with the result,

$$\boxed{\mathbb{B}_1 \phi := \frac{\partial \phi}{\partial n} + \frac{1}{R}\phi + \frac{1}{c}\dot{\phi} = 0} \tag{5.19}$$

This condition is perfectly absorbing for axially symmetric spherical waves (outgoing wave harmonic $n = 0$).

Second-order boundary condition

For $N = 2$, the system (5.13) yields, $\beta_0 = z_0$ and $\beta_1 = (z_1 - z_0)/2$, so that (5.14) becomes,

$$\frac{\partial \phi}{\partial n} = z_0 \phi + \frac{1}{2}(z_0 - z_1)\Delta_\Gamma \phi \tag{5.20}$$

Clearing the common denominator $h_0 h_1$ we obtain,

$$h_0 h_1 \frac{\partial \phi}{\partial n} = (k h_0' h_1)\phi + \frac{k}{2}(h_0' h_1 - h_1' h_0)\Delta_\Gamma \phi \tag{5.21}$$

Using the recurrence relation,

$$h_n' = h_{n-1} - \left(\frac{n+1}{kR}\right) h_n\,, \qquad n = 1, 2, \cdots \tag{5.22}$$

in conjunction with the starting functions defined in (5.16), and after some algebraic manipulation, we obtain the simplified form,

$$\left(\frac{1}{R} - ik\right)\frac{\partial \phi}{\partial n} \quad = \quad \left(k^2 + \frac{2ik}{R} - \frac{1}{R^2}\right)\phi + \frac{1}{2R^2}\Delta_\Gamma \phi \tag{5.23}$$

Since this expression involves only terms in powers of $(ik)^j$, the inverse Fourier transform is readily obtained with the desired result,

$$\boxed{\mathbb{B}_2\phi := \frac{\partial\phi}{\partial n} + \frac{R}{c}\frac{\partial\dot{\phi}}{\partial n} + \frac{R}{c^2}\ddot{\phi} + \frac{2}{c}\dot{\phi} + \frac{1}{R}\phi - \frac{1}{2R}\Delta_\Gamma\phi = 0} \tag{5.24}$$

This higher-order accurate local boundary condition is perfectly absorbing for the first two spherical wave harmonics of orders $n = 0$ and $n = 1$.

Third-order boundary condition

For $N = 3$, (5.14) becomes,

$$\frac{\partial\phi}{\partial n} = \beta_0\phi - \beta_1\Delta_\Gamma\phi + \beta_2(\Delta_\Gamma)^2\phi \tag{5.25}$$

and the system (5.13) yields the three coefficients,

$$\begin{aligned} \beta_0 &= z_0 \\ \beta_1 &= (18z_1 - 16z_0 - 2z_2)/24 \\ \beta_2 &= (2z_0 + z_2 - 3z_1)/24 \end{aligned}$$

Using the recurrence relation (5.22), and

$$h_{n+1} = \frac{(2n+1)}{kR}h_n - h_{n-1}\,, \qquad n = 1, 2, \cdots \tag{5.26}$$

in conjunction with the starting functions defined in (5.16), or equivalently (5.8), we obtain the simplified form,

$$\gamma_0\phi_{,n} = \gamma_1\phi + \gamma_2\Delta_\Gamma\phi + \gamma_3(\Delta_\Gamma)^2\phi \tag{5.27}$$

where the frequency dependent coefficients are

$$\gamma_0 = 1 - 2ikR - 4(kR)^2/3 + i(kR)^3/3$$

$$\begin{aligned}
\gamma_1 &= -1/R + 3ik + 10k^2R/3 - 5ik^3R^2/3 - k^4R^3/3 \\
\gamma_2 &= 7/(12R) - ik/2 - k^2R/6 \\
\gamma_2 &= 1/(24R)
\end{aligned}$$

Since (5.27) involves only terms in powers of $(ik)^j$, the inverse Fourier transform is readily obtained with the desired result,

$$\begin{aligned}
\mathbb{B}_3\phi \;:=\; & \phi_{,n} + \frac{2R}{c}\phi_{,nt} + \frac{4R^2}{3c^2}\phi_{,ntt} + \frac{R^3}{c^3}\phi_{,nttt} \\
& + \frac{1}{R}\phi + \frac{3}{c}\phi_{,t} + \frac{10R}{3c^2}\phi_{,tt} + \frac{5R^2}{3c^3}\phi_{,ttt} + \frac{R^3}{3c^4}\phi_{,tttt} \\
& - \frac{7}{12R}\Delta_\Gamma\phi - \frac{1}{2c}\Delta_\Gamma\phi_{,t} - \frac{R}{6c^2}\Delta_\Gamma\phi_{,tt} - \frac{1}{24R}(\Delta_\Gamma)^2\phi = 0
\end{aligned} \tag{5.28}$$

In this expression an inferior comma denotes differentiation. This higher-order accurate local boundary condition is perfectly absorbing for the first three spherical wave harmonics of orders $n = 0, 1$ and $n = 2$. Expressions for the exact time-dependent local boundary conditions for higher-order modes $N = 4, 5, \cdots$, are obtained using the same procedure as indicated for $N = 1, 2, 3$.

5.2.2 Finite element implementation

Defining the linear operator $\mathbb{S}_m$ as,

$$\mathbb{B}_m(\phi) := \frac{\partial\phi}{\partial n} + \mathbb{S}_m(\phi) \tag{5.29}$$

which implies

$$\frac{\partial\phi}{\partial n} = -\mathbb{S}_m\phi \qquad \text{on} \quad \Gamma_\infty \tag{5.30}$$

we obtain boundary conditions expressed in the form of (3.25) relating Dirchlet-to-Neumann data through local differential operators. For example, the first three local operators $\mathbb{S}_m$ for m equal to 1,2 and 3 are:

$$\mathbb{S}_1\phi = \frac{1}{R}\phi + \frac{1}{c}\phi_{,t} \tag{5.31}$$

$$\mathbb{S}_2\phi = \frac{1}{2R}(2-\Delta_\Gamma)\phi + \frac{1}{c}\left(2+R\frac{\partial}{\partial r}\right)\phi_{,t} + \frac{R}{c^2}\phi_{,tt} \tag{5.32}$$

$$\begin{aligned}\mathbb{S}_3\phi &= \frac{1}{24R}(24-14\Delta_\Gamma-(\Delta_\Gamma)^2)\phi + \frac{1}{2c}\left(6-\Delta_\Gamma+4R\frac{\partial}{\partial r}\right)\phi_{,t} \\ &+ \frac{R}{6c^2}\left(20-\Delta_\Gamma+8R\frac{\partial}{\partial r}\right)\phi_{,tt} + \frac{R^2}{3c^3}\left(5+3R\frac{\partial}{\partial r}\right)\phi_{,ttt} + \frac{R^3}{3c^4}\phi_{,tttt}\end{aligned} \tag{5.33}$$

This sequence of local time-dependent boundary conditions provide increasing accuracy with order N which, however, is also a measure of the difficulty of implementation. In general, the Nth-order condition contains all the even tangential and temporal derivatives up to order $2(N-1)$. For example, for the case $N=2$, the local time-dependent operator (5.32) contains second-order tangential derivatives embedded in the Laplace-Beltrami operator Δ_Γ and second-order time derivatives. Similarly, for $N=3$, the local operator (5.33) contains fourth-order tangential derivatives and fourth-order temporal derivatives. As a result of the higher-order time derivatives, these boundary operators become increasingly difficult to implement in a semidiscrete finite element formulation using standard time-integrators such as the Newmark family. A distinct advantage of the time-discontinuous space-time formulation is that it allows the solution at time t_n to be discontinuous across space-time slabs on the truncation boundary $(\Upsilon_\infty)_n := \Gamma_\infty \times I_n$. As a result, standard C^0 continuous finite element interpolation functions in the temporal variable may be used up to the order dictated by the time-derivatives appearing in the boundary operator. For example, for $N=2$, standard C^0 quadratic Lagrangian interpolation functions can be used to represent the second-order time derivative appearing in (5.32). For this, standard C^0 interpolations can also be used to represent the tangential derivates appearing in the Laplace-Beltrami operator after integrating by parts on Γ_∞.

The sequence of boundary operators defined in (5.31) through (5.33) are incorporated into the space-time finite element formulation as natural boundary conditions, i.e. they are weakly enforced in both time and space. The weak enforcement of $\mathbb{S}_1$ has been described previously in the definition for the acoustic intensity operator given in (3.29) - (3.31). For $\mathbb{S}_2$, the general form of the acoustic intensity operator defined

in (3.33), specializes to

$$\begin{aligned} d_0(\dot{w}^h\,,\,\phi^h)_{(\Upsilon_\infty)_n} &= \frac{1}{R}(\dot{w}^h\,,\,\phi^h)_{(\Upsilon_\infty)_n} + \frac{1}{2R}(\dot{w}^h_{,\varphi}\,,\,\phi^h_{,\varphi})_{(\Upsilon_\infty)_n} \\ &+ \frac{1}{2R}(\dot{w}^h_{,\theta}\,,\,\csc^2(\varphi)\,\phi^h_{,\theta})_{(\Upsilon_\infty)_n} \end{aligned} \tag{5.34}$$

$$d_1(\dot{w}^h\,,\,\dot{\phi}^h)_{(\Upsilon_\infty)_n} = \frac{2}{c}(\dot{w}^h\,,\,\dot{\phi}^h)_{(\Upsilon_\infty)_n} + \frac{R}{c}(\dot{w}^h\,,\,\dot{\phi}^h_{,r})_{(\Upsilon_\infty)_n} \tag{5.35}$$

$$d_2(\dot{w}^h\,,\,\ddot{\phi}^h)_{(\Upsilon_\infty)_n} = \frac{R}{c^2}(\dot{w}^h\,,\,\ddot{\phi}^h)_{(\Upsilon_\infty)_n} \tag{5.36}$$

In (5.34), tangential continuity is relaxed on the boundary Γ_∞ through integration by parts:

$$(w\,,\,\Delta_\Gamma\phi)_{\Gamma_\infty} = -(w_{,\varphi}\,,\,\phi_{,\varphi})_{\Gamma_\infty} - (w_{,\theta}\,,\,\csc^2(\varphi)\,\phi_{,\theta})_{\Gamma_\infty} \tag{5.37}$$

Since these boundary operators are local in space and time, the sparse data structure of the finite element arrays is preserved. The locality in time enables the use of only local causal updates from one time step to the next. Thus local boundary conditions of this type have a distinct advantage in computational storage when compared to competing approaches, e.g. Kirchoff's retarded potential representation or the direct convolution of the DtN map (5.7), which involves a temporal integral over all past time and leads to numerical formulations that can be extremely memory-intensive, typically requiring storage of a large pool of historical data.

Temporal continuity across space-time slabs is weakly enforced through the temporal jump operators embedded in the operators $d_2(\cdot\,,\,\cdot)_{\Gamma_\infty}$ and $d_0(\cdot\,,\,\cdot)_{\Gamma_\infty}$, defined in (3.26). For $\mathbb{S}_1$, the consistent jump terms are given in (3.34). For $\mathbb{S}_2$, the consistent jump terms specialize to,

$$\begin{aligned} d_0(w^h(t_n^+)\,,\,[\![\phi^h(t_n)]\!])_{\Gamma_\infty} &= \frac{1}{R}(w^h(t_n^+)\,,\,[\![\phi^h(t_n)]\!])_{\Gamma_\infty} \\ &+ \frac{1}{2R}(w^h_{,\varphi}(t_n^+)\,,\,[\![\phi^h_{,\varphi}(t_n)]\!])_{\Gamma_\infty} \\ &+ \frac{1}{2R}(w^h_{,\theta}(t_n^+)\,,\,\csc^2(\varphi)\,[\![\phi^h_{,\theta}(t_n)]\!])_{\Gamma_\infty} \end{aligned} \tag{5.38}$$

$$d_2(\dot{w}^h(t_n^+)\,,\,[\![\dot{\phi}^h(t_n)]\!])_{\Gamma_\infty} = \frac{R}{c^2}(\dot{w}^h(t_n^+)\,,\,[\![\dot{\phi}^h(t_n)]\!])_{\Gamma_\infty} \tag{5.39}$$

Remarks

1. As discussed in Section 3.4.2, the first-order operator $\mathbb{S}_1$, satisfies the positivity property given in (3.35). The second-order operator $\mathbb{S}_2$, satisfies the positivity property for all terms up to the nonsymmetric operator in the second term of (5.35). As a result, the stability estimate derived earlier in Theorem (4.1), does not strictly hold. While stability is difficult to prove *a priori* through a rigorous functional analysis for this case, extensive numerical studies in Section 5.3 indicate that the operator $\mathbb{S}_2$ is indeed stable for all the numerical examples run to date. These good results suggest that a rigorous proof of stability for this boundary operator should be possible.

2. Because the space-time formulation allows for the use of C^0 interpolations to represent the high-order time derivatives, it is possible to implement the time-dependent operators to any order desired to obtain higher-order accurate non-reflecting boundary conditions. However for operators in the sequence extending beyond $N \geq 3$, the lowest possible order of spatial continuity on the artificial boundary that can be achieved after integration by parts is C^{N-2}. In this case a layer of boundary elements adjacent to Γ_∞, possessing high-order tangential continuity on Γ_∞ are needed. For example, for $N = 3$, C^1 continuous interpolation functions, e.g. Hermite polynomials, are needed to represent the second-order tangential derivatives appearing in the weak enforcement of $\mathbb{S}_3$. It is this potential limitation that motivated the derivation of the local in time and nonlocal in space version of the boundary conditions discussed in the next section, where no requirement on higher-order continuity is present.

3. An interesting observation is that the first-order operator $\mathbb{B}_1$ coincides with the well known spherical damper and is equivalent to the first local boundary condition in the sequence derived by Bayliss and Turkel [1980] and Engquist and Majda [1977]. In addition, we observe that our local boundary condition $\mathbb{B}_2$, which is exact for the first two spherical wave harmonics, coincides with the second-order boundary condition derived by Bayliss and Turkel [1980], after the higher-order radial derivatives in the Bayliss and Turkel sequence are eliminated in favor of high-order tangential derivatives through use of the wave equation in three-dimensions. The equivalence of this second-order

operator holds in both the time-dependent and time-harmonic cases. However for $N \geq 3$, our non-reflecting boundary conditions are different than those of Bayliss and Turkel. Another sequence of time-dependent non-reflecting boundary conditions that is closely related to ours is given in GROTE AND KELLER [1994].

4. An alternative form of the boundary conditions $\mathbb{S}_m$ can be obtained by replacing the high-order temporal derivatives appearing in the operator with high-order radial and tangential derivatives through repeated use of the wave equation written in separable coordinates, e.g. for a sphere in three-dimensions,

$$\frac{\partial^2 \phi}{\partial t^2} = \left(\frac{c}{r}\right)^2 \left[\frac{\partial}{\partial r}\left(r^2 \frac{\partial \phi}{\partial r}\right) + \Delta_\Gamma \phi\right] \tag{5.40}$$

evaluated at $r = R$. However in this approach, the implementation of high-order radial derivatives is not natural to the standard finite element method, and is not recommended.

5.2.3 Local in time and nonlocal in space version

In order to obtain non-reflecting boundary conditions which possess the important property of locality in time, without the requirement of high-order tangential continuity in the Laplace-Beltrami operator $(\Delta_\Gamma)^j$, a local in time counterpart to the spatially nonlocal DtN map (5.2) is derived which exactly represents the first N spherical wave harmonics. This new sequence of boundary conditions retains the nonlocal spatial integral, yet replaces the temporal integral of the time-convoluted DtN map with higher-order local time derivatives. Thus this new sequence of time-dependent boundary conditions has the advantage that when implemented in the space-time formulation, standard C^0 interpolation functions may be used for both the space and time variables.

First-order boundary condition

Consider the first term in the truncated DtN series with $N = 1$, then (5.2) reduces to,

$$\frac{\partial \phi}{\partial n} = z_0 \int_{\Gamma_\infty} \phi \, s_0 \, d\Gamma' \tag{5.41}$$

where $s_0 = 1/(4\pi R^2)$ and $z_0 = kh_0'/h_0$. Using (5.16) and (5.8) and clearing the denominator h_0 gives the alternate form,

$$\frac{\partial \phi}{\partial n} \quad = \quad \left(ik - \frac{1}{R}\right) \int_{\Gamma_\infty} \phi \, s_0 \, d\Gamma' \tag{5.42}$$

Taking the inverse Fourier transform we obtain the local in time but nonlocal in space boundary condition,

$$\mathbb{B}_1 \phi := \frac{\partial \phi}{\partial n} + \int_{\Gamma_\infty} \left(\frac{1}{c}\dot{\phi} + \frac{1}{R}\phi\right) s_0 \, d\Gamma' = 0 \tag{5.43}$$

This condition is perfectly absorbing for axially symmetric spherical waves (outgoing wave harmonic $n = 0$).

Second-order boundary condition

For $N = 2$, the first two terms in the truncated DtN series (5.2) take the form,

$$\frac{\partial \phi}{\partial n} \quad = \quad z_0 \int_{\Gamma_\infty} \phi \, s_0 \, d\Gamma' + z_1 \int_{\Gamma_\infty} \phi \, s_1 \, d\Gamma' \tag{5.44}$$

Using the definition for z_n and relations (5.16),(5.22), (5.8) and clearing the common denominator $h_0 h_1$ we obtain the alternative form,

$$\left(\frac{1}{R} - ik\right) \frac{\partial \phi}{\partial n} \quad = \quad \left(k^2 + \frac{2ik}{R} - \frac{1}{R^2}\right) \int_{\Gamma_\infty} \phi \, s_0 \, d\Gamma' + \left(k^2 + \frac{2ik}{R} - \frac{2}{R^2}\right) \int_{\Gamma_\infty} \phi \, s_1 \, d\Gamma' \tag{5.45}$$

Taking the inverse Fourier transform we arrive at the time-dependent counterpart to (5.45):

$$\begin{aligned} \mathbb{B}_2 \phi := \frac{\partial \phi}{\partial n} + \frac{R}{c}\frac{\partial \dot{\phi}}{\partial n} \quad &+ \quad \int_{\Gamma_\infty} \left(\frac{R}{c^2}\ddot{\phi} + \frac{2}{c}\dot{\phi} + \frac{1}{R}\phi\right) s_0 \, d\Gamma' \\ &+ \quad \int_{\Gamma_\infty} \left(\frac{R}{c^2}\ddot{\phi} + \frac{2}{c}\dot{\phi} + \frac{2}{R}\phi\right) s_1 \, d\Gamma' = 0 \end{aligned} \tag{5.46}$$

where s_0 and s_1 are defined in (5.3). This condition is perfectly absorbing for the first two spherical wave harmonics of order $n = 0$ and $n = 1$.

Third-order boundary condition

For $N = 3$, the first three terms in the truncated DtN series (5.2) are,

$$\frac{\partial \phi}{\partial n} = z_0 \int_{\Gamma_\infty} \phi\, s_0\, d\Gamma' + z_1 \int_{\Gamma_\infty} \phi\, s_1\, d\Gamma' + z_2 \int_{\Gamma_\infty} \phi\, s_2\, d\Gamma' \tag{5.47}$$

Using the definition for z_n, the relations (5.16),(5.22), (5.8) and clearing the common denominator $h_0 h_1 h_2$ we obtain the alternative form,

$$\gamma_0 \frac{\partial \phi}{\partial n} = \gamma_1 \int_{\Gamma_\infty} \phi\, s_0\, d\Gamma' + \gamma_2 \int_{\Gamma_\infty} \phi\, s_1\, d\Gamma' + \gamma_3 \int_{\Gamma_\infty} \phi\, s_2\, d\Gamma' \tag{5.48}$$

where

$$\begin{aligned}
\gamma_0 &= 1 - 2ikR - 4(kR)^2/3 + i(kR)^3/3 \\
\gamma_1 &= -1/R + 3ik + 10k^2R/3 - 5ik^3R^2/3 - k^4R^3/3 \\
\gamma_2 &= -2/R + 4ik + 11k^2R/3 - 5ik^3R^2/3 - k^4R^3/3 \\
\gamma_3 &= -3/R + 6ik + 13k^2R/3 - 5ik^3R^2/3 - k^4R^3/3
\end{aligned}$$

Taking the inverse Fourier transform gives the time-dependent counterpart:

$$\mathbb{B}_3\phi := \phi_{,n} + \frac{2R}{c}\phi_{,nt} + \frac{4R^2}{3c^2}\phi_{,ntt} + \frac{R^3}{3c^3}\phi_{,nttt} \tag{5.49}$$

$$\begin{aligned}
&+ \int_{\Gamma_\infty} \left(\frac{R^3}{3c^4}\phi_{,tttt} + \frac{5R^2}{3c^3}\phi_{,ttt} + \frac{10R}{3c^2}\phi_{,tt} + \frac{3}{c}\phi_{,t} + \frac{1}{R}\phi \right) s_0\, d\Gamma' \\
&+ \int_{\Gamma_\infty} \left(\frac{R^3}{3c^4}\phi_{,tttt} + \frac{5R^2}{3c^3}\phi_{,ttt} + \frac{11R}{3c^2}\phi_{,tt} + \frac{4}{c}\phi_{,t} + \frac{2}{R}\phi \right) s_1\, d\Gamma' \\
&+ \int_{\Gamma_\infty} \left(\frac{R^3}{3c^4}\phi_{,tttt} + \frac{5R^2}{3c^3}\phi_{,ttt} + \frac{13R}{3c^2}\phi_{,tt} + \frac{6}{c}\phi_{,t} + \frac{3}{R}\phi \right) s_2\, d\Gamma' = 0
\end{aligned} \tag{5.50}$$

where $s_n, \quad n = 0, 1, 2$ are defined in (5.3). This condition is perfectly absorbing for the first three spherical wave harmonics of order $n = 0, 1, 2$. Local in time counterparts for the higher terms, $N \geq 4$, in the truncated DtN series are obtained following the same procedure outlined for $N = 1, 2, 3$. These are nonlocal operators that involve

a spatial integral yet retain the important property of locality in time. In general, the boundary operators in this sequence will have higher-order time derivatives up to $2(N-1)$. By expressing the boundary operators in the form,

$$\mathbb{B}_m(\phi) := \frac{\partial \phi}{\partial n} + \mathbb{S}_m(\phi) \tag{5.51}$$

which implies,

$$\frac{\partial \phi}{\partial n} = -\mathbb{S}_m \phi \qquad \text{on} \quad \Gamma_\infty \tag{5.52}$$

the sequence of boundary operators can be implemented as natural boundary conditions in the space-time formulation. The implementation follows a similar procedure to that in Section 5.2.2 where the operator $\mathbb{S}_m$ is weakly enforced through the acoustic intensity operator defined in (3.26).

The advantage of this sequence of operators is that when implemented in the discontinuous space-time finite element formulation, standard C^0 continuous interpolations may be used on $\Gamma_\infty \times I_n$ in both the space and time dimensions. For example, for the third-order operator $\mathbb{B}_3$ defined in (5.50), standard C^0 quartic basis functions in the time dimension and C^0 linear basis functions in the spatial dimension may be used to interpolate the fourth-order temporal and first-order spatial derivatives appearing in the boundary operator. This feature circumvents the need for high-order continuous tangential interpolation functions as required by the local in space version described earlier in Section 5.2.1 for orders $N \geq 3$. It is this special property of the local in time and nonlocal in space version of the non-reflecting boundary conditions, when implemented in the time-discontinuous formulation which offers the greatest potential for implementation of high-order boundary conditions beyond second-order. A closely related sequence can be found in Grote and Keller [1994].

5.3 Numerical Examples

In this section a large number of numerical examples are conducted to demonstrate the effectiveness of the time-discontinuous Galerkin space-time finite element method to accurately model transient acoustic radiation. The problems investigated are primarily designed to assess the performance of the local non-reflecting boundary conditions when implemented in the time-discontinuous Galerkin variational formulation. Only

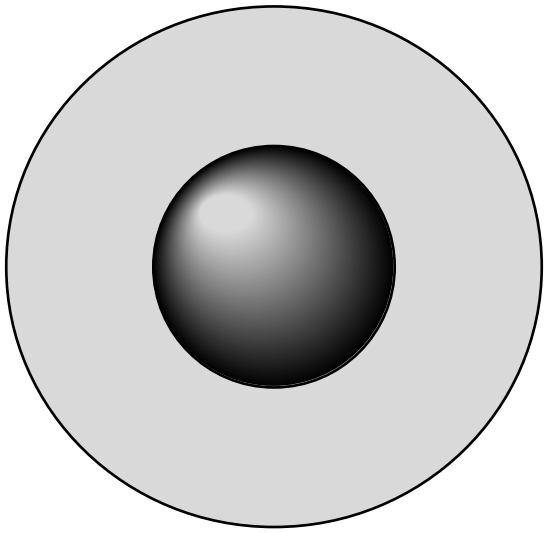

Figure 5.3: Sphere of radius $r = a$ enclosed by a spherical artificial boundary of radius $R = 2a$.

results for the local in time and local in space version of the non-reflecting boundary operators defined in Section 5.2.1 are given. Comparisons are made with the PW-damper $\mathbb{S}_0$ defined in (2.24), and the first-order $\mathbb{S}_1$, and second-order $\mathbb{S}_2$, local boundary conditions defined in (5.31) and (5.32) respectively. For all the numerical results presented, the GLS mesh parameters are set to zero and standard C^0 quadratic finite element shape functions are used in both the time and space dimensions.

All computations were performed on a Sun-SPARCstation 2, in double-precision, and $2 \times 2 \times 2$ Gaussian quadrature for tri-quadratic space-time domain elements and 2×2 quadrature for bi-quadratic space-time boundary elements. To this authors knowledge, this is the first implementation of the time-discontinuous Galerkin space-time finite element method for second-order hyperbolic equations in multidimensions. Numerical results for one-dimensional problems (without non-reflecting boundaries) are reported in Hulbert and Hughes [1989,1990].

5.3.1 Spherical harmonic radiation

In this example, consider the time-dependent radiation from a sphere of radius $r = a$, with a harmonic load distribution of the form,

$$\phi(a, \varphi, t) = P_n(\cos\varphi)\sin\omega t, \qquad \text{for } 0 \le \varphi < \pi\,, \quad t > 0 \tag{5.53}$$

The exact steady-state solution for this problem is,

$$\phi(r, \varphi, t) = -\text{Imag}\left\{\frac{h_n(kr)}{h_n(ka)} P_n(\cos\varphi)\mathrm{e}^{-i\omega t}\right\} \qquad \text{for } r \ge a \tag{5.54}$$

where P_n are Legendre polynomials of the first kind and h_n are spherical Hankel functions of the first kind of order n. When using a finite element method incorporating approximate non-reflecting boundary conditions on a spherical artificial boundary as illustrated in Figure 5.3, this problem becomes increasingly difficult to solve as the wave harmonic n increases. The spherically symmetric damper $\mathbb{S}_1$ defined in (3.28) or (5.31) is exact for the breathing mode, which corresponds to the harmonic $n = 0$. However, for higher modes, $n = 1, 2, \cdots$ this condition is only approximate. An improved approximation is obtained by using the second-order operator $\mathbb{S}_2$ derived in (5.32). This time-dependent boundary condition is exact for the first two spherical harmonics, $n = 0, 1$.

For this axisymmetric problem, the computational domain is taken as $\Omega = \{a < r < R, 0 \le \varphi < \pi\}$. with the truncation boundary set at $R = 2a$. The resulting bounded domain Ω is discretized with 400 axisymmetric acoustic elements: 10 elements in the radial direction, and 40 elements in the polar direction, see Figure 5.4. As a consequence of the axisymmetric nature of the problem, there is no circumferential dependence on the solution and all terms which depend on the coordinate θ are neglected in the definition of the non-reflecting boundary conditions. In particular, for the local boundary operator $\mathbb{S}_2$ defined in (5.32), the third term in (5.34) and (5.38) are neglected.

A series of transient space-time finite element solutions were obtained for the axisymmetric loading (5.53) with harmonics ranging from $n = 0$ through $n = 4$. A time-increment of $\Delta t = 0.1$ with zero initial conditions on ϕ and $\dot{\phi}$ was used for all the examples in this section. The system starts from rest and is driven towards the steady-state solution with time.

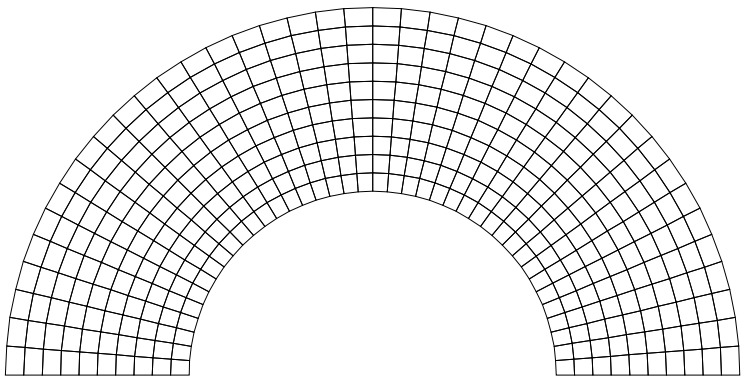

Figure 5.4: Axisymmetric mesh with 400 quadratic elements.

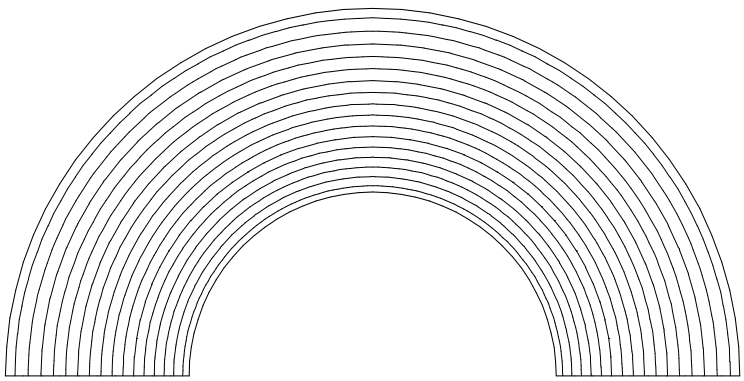

Figure 5.5: Breathing mode ($n = 0$) for a radiating sphere: Solution contours at time $t = 30$ and normalized frequency $ka = 1$.

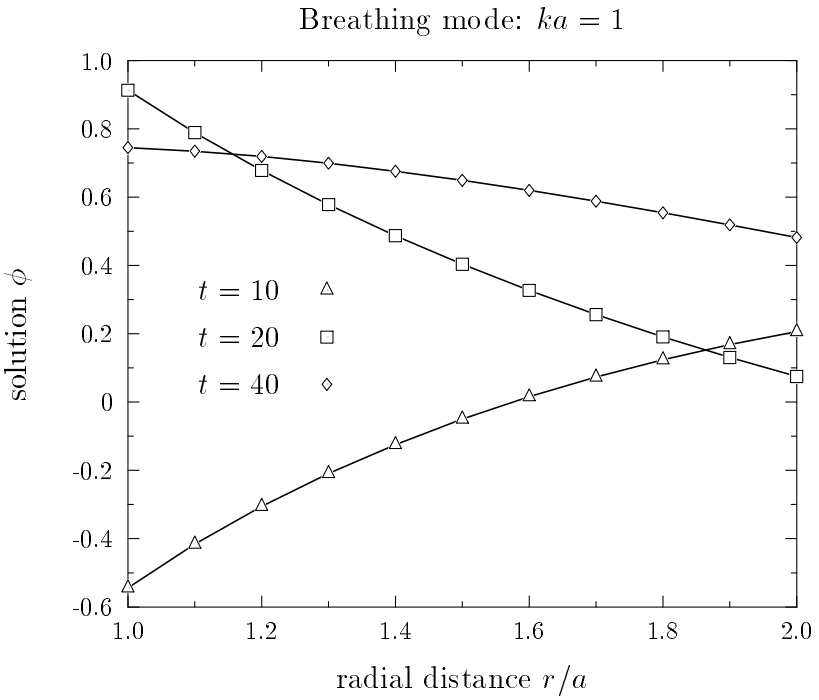

Figure 5.6: Breathing mode ($n = 0$) for a radiating sphere: $ka = 1$. Solution profile using S_1 local boundary condition along the radial distance $a < r < R$, at times $t = 10, 20, 40$.

Harmonic $n = 0$:

Before proceeding to more complex radiation patterns we wish to confirm that the spherical operator $\mathbb{S}_1$, is exact for the 'breathing' mode $n = 0$, i.e. for the radiation loading $P_0(\cos\varphi)\sin\omega t$. Figure 5.5 illustrates the contours for the space-time solution at $t = 30$ and a normalized frequency $ka = 1$. Figure 5.6 shows a profile of the time-dependent space-time solution after reaching steady-state in comparison to the exact time-harmonic solution (5.54). The solutions are plotted along the radial coordinate at three sample times: $t = 10, 20, 40$. The solution sample times are such that many spurious reflections between the artificial boundary $r = R$, and the radiating surface at $r = a$, could have occurred. From these results it is clear that the $\mathbb{S}_1$ operator when implemented in the discontinuous Galerkin formulation gives nearly exact solutions for the $n = 0$ spherical harmonic as expected. Numerical results for other values of ka support this conclusion (not shown).

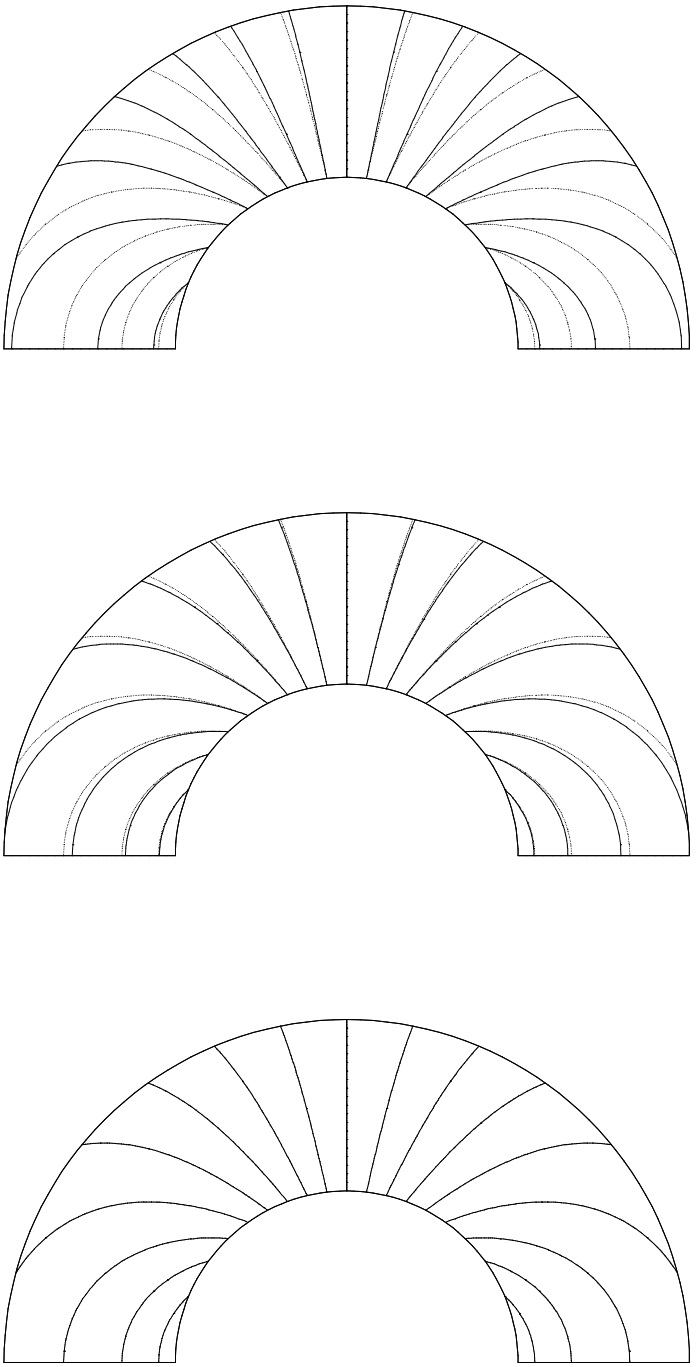

Figure 5.7: Radiation from a sphere with polar harmonic $n = 1$ and normalized frequency $ka = 1$. Contours of space-time solution at $t = 20$ using local boundary conditions, (Top): 'plane-wave' S_0, (Middle): first-order S_1, (Bottom): second-order S_2. (dotted contours denote analytical solution).

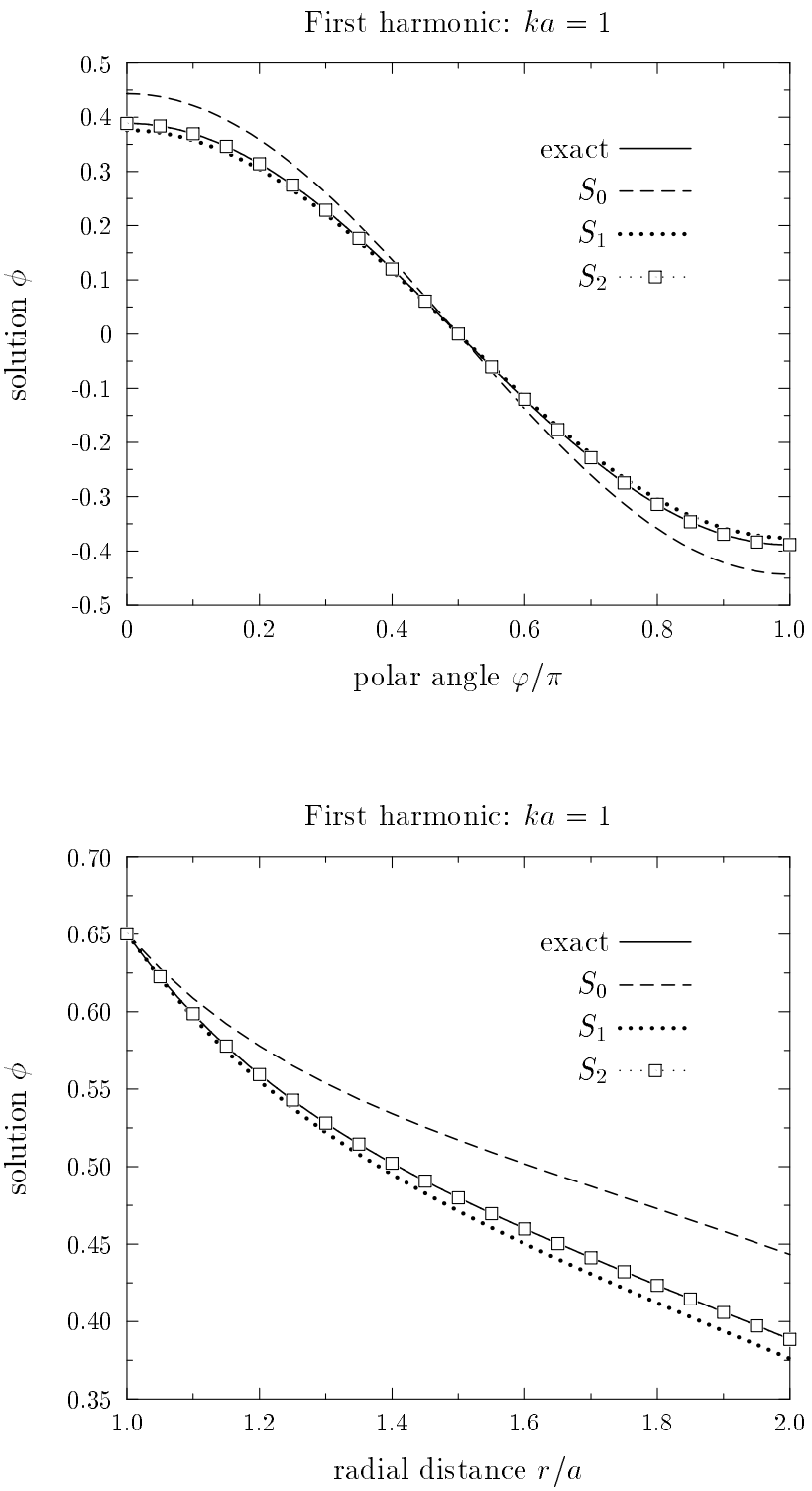

Figure 5.8: Spherical wave harmonic $n = 1$: Results at $t = 20$, comparing the 'plane-wave' S_0, first-order S_1, and second-order S_2 boundary conditions. (Top): Solution profile on the artificial boundary $r = R$. (Bottom): Solution plotted along radial line at $\varphi = 0$.

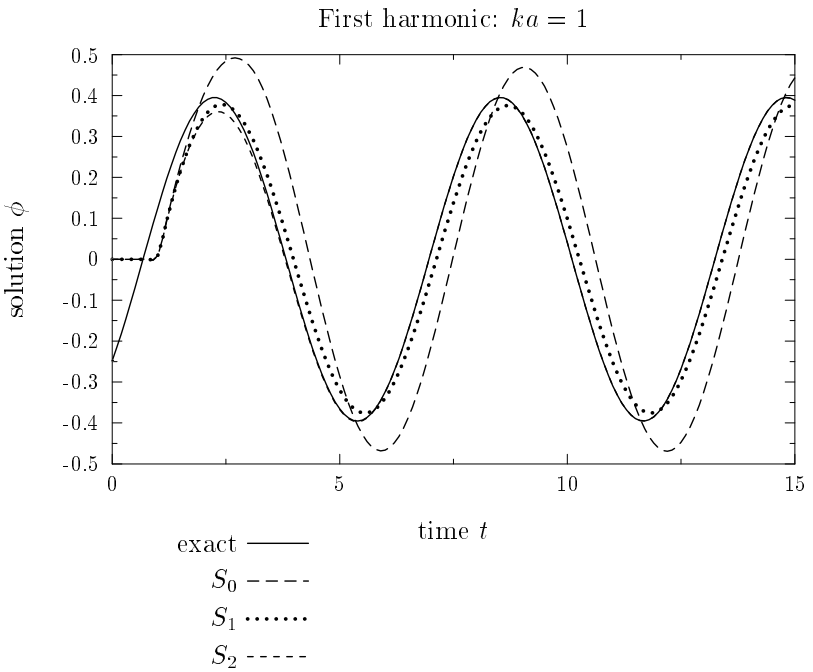

Figure 5.9: Time-dependent solution at a point on the artificial boundary, i.e. $r = R$ and $\varphi = 0$. Results show the transient solution as it is driven to steady-state.

Harmonic $n = 1$:

To verify that the second-order boundary operator $\mathbb{S}_2$ is exact for the second wave harmonic, $n = 1$, the numerical solution is obtained for the loading $P_1(\cos\varphi)\sin\omega t$ and $ka = 1$. Figure 5.7 illustrates the contours of the discontinuous Galerkin solution incorporating the local 'plane-wave' boundary operator, $\mathbb{S}_0$, defined in (2.24), and the first-order $\mathbb{S}_1$, and second-order $\mathbb{S}_2$, boundary operators defined in (5.31) and (5.32) respectively, in comparison to the exact steady-state solution. Figure 5.8 shows the solution profile around the artificial boundary at $r = R$, as well as the solution plotted along a radial line located at the polar angle $\varphi = 0$. Figure 5.9 shows the time-dependent solution at a point on the artificial boundary at position $(r, \varphi) = (R, 0)$. Results confirm that the local operator $\mathbb{S}_2$, when implemented in the space-time formulation, give nearly exact solutions for harmonic $n = 1$. The numerical solution using $\mathbb{S}_1$ is somewhat out-of-phase with the exact steady-state solution while the simple 'plane-wave' damper $\mathbb{S}_0$, shows significant errors in both phase and amplitude.

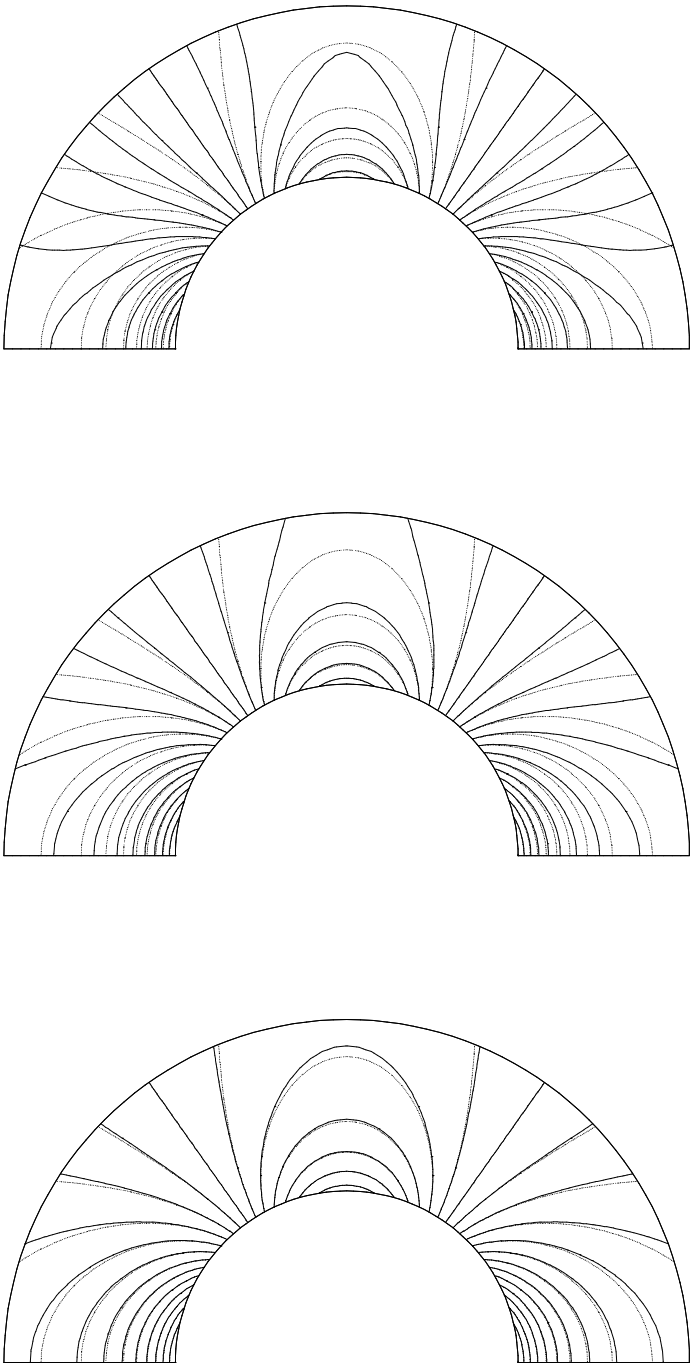

Figure 5.10: Radiation from sphere with polar harmonic $n = 2$ and normalized frequency $ka = 1$. Contours of space-time solution using local boundary conditions, (Top): 'plane-wave' S_0, (Middle): first-order S_1, (Bottom): second-order S_2. (dotted contours denote analytical solution).

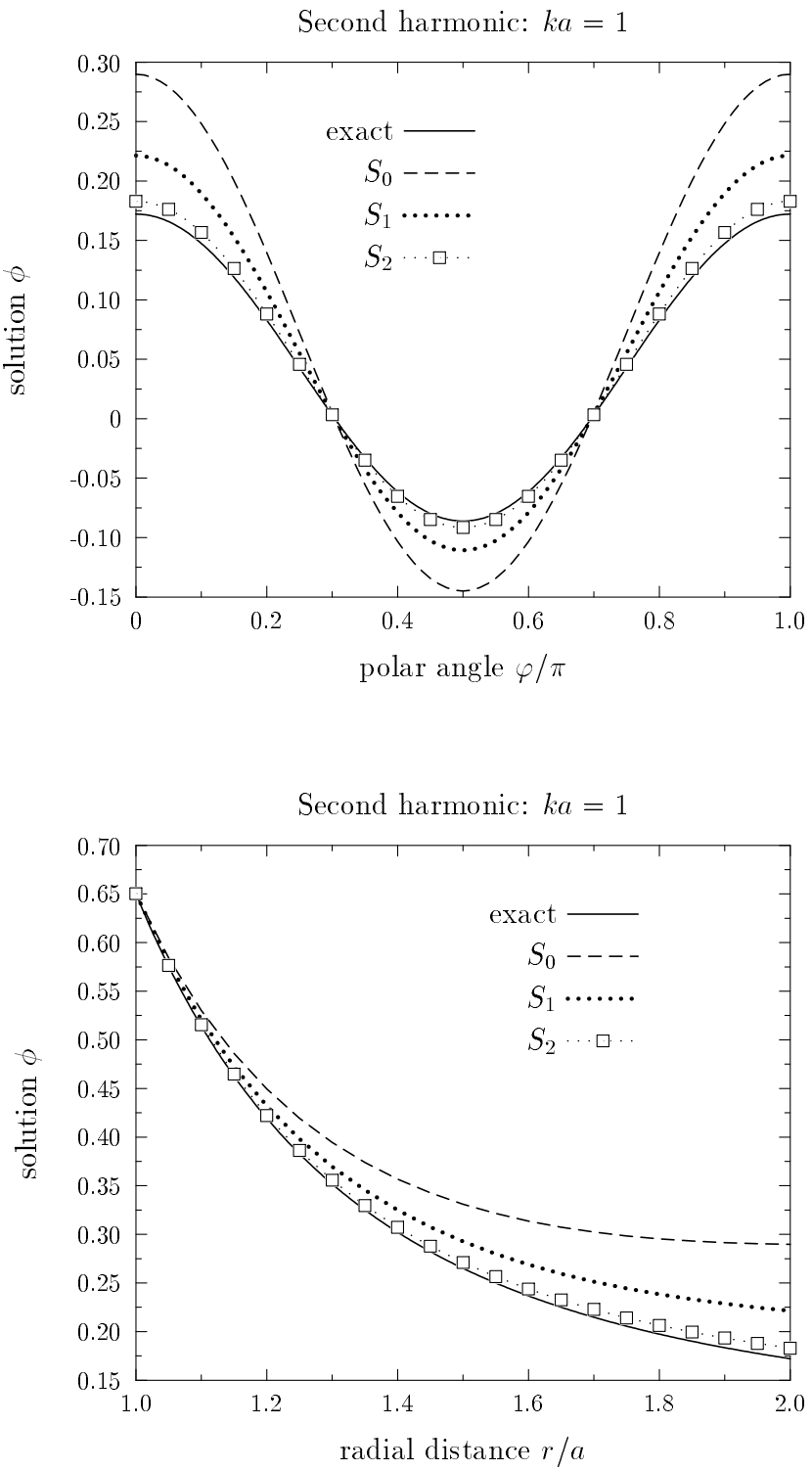

Figure 5.11: Spherical wave harmonic $n = 2$: Results comparing the 'plane-wave' S_0, first-order S_1, and second-order S_2, boundary conditions. (Top): Solution profile on the artificial boundary $r = R$. (Bottom): Solution plotted along radial line at $\varphi = 0$.

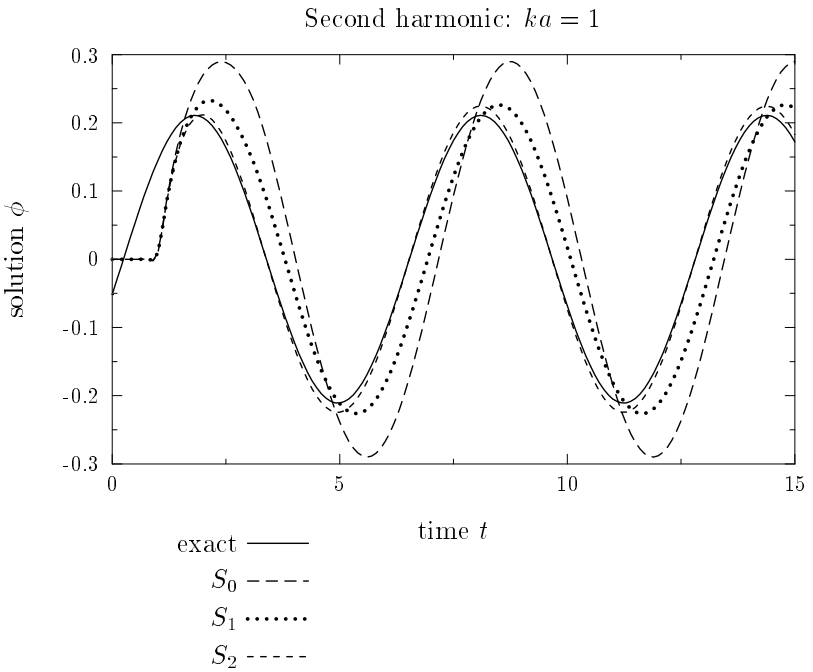

Figure 5.12: Time-dependent solution at a point on the artificial boundary, i.e. $r = R$ and $\varphi = 0$. Results show the transient solution as it is driven to steady-state.

Harmonic $n = 2$:

To demonstrate the effectiveness of the second-order operator $\mathbb{S}_2$ to yield accurate numerical solutions for higher modes, we examine harmonic $n = 2$, for a driving frequency given by the nondimensional wavenumber $ka = 1$. Figures 5.10 and 5.11 show a comparison of the space-time solution at time $t = 15$, using the local boundary operators $\mathbb{S}_j$, $j = 0, 1, 2$, The numerical results using the low-order operators $\mathbb{S}_0$ and $\mathbb{S}_1$ show a significant error in the solution, while the solution using $\mathbb{S}_2$ remains relatively accurate with only a small error in amplitude, see Figure 5.12.

Harmonic $n = 3$:

Numerical solutions for harmonic loading with $n = 3$, with a driving frequency of $ka = 1$ show significant error for all three local boundary operators tested. However, by increasing the nondimensional wavenumber to $ka = 3$, i.e. by setting the driving frequency to $\omega = 1$ with a wave speed $c = 1/3$, we observe accurate results using the second-order operator $\mathbb{S}_2$. Figures 5.13 through 5.14 show the space-time solution for this frequency. Results using $\mathbb{S}_0$ and $\mathbb{S}_1$ show significant error in the solution. In

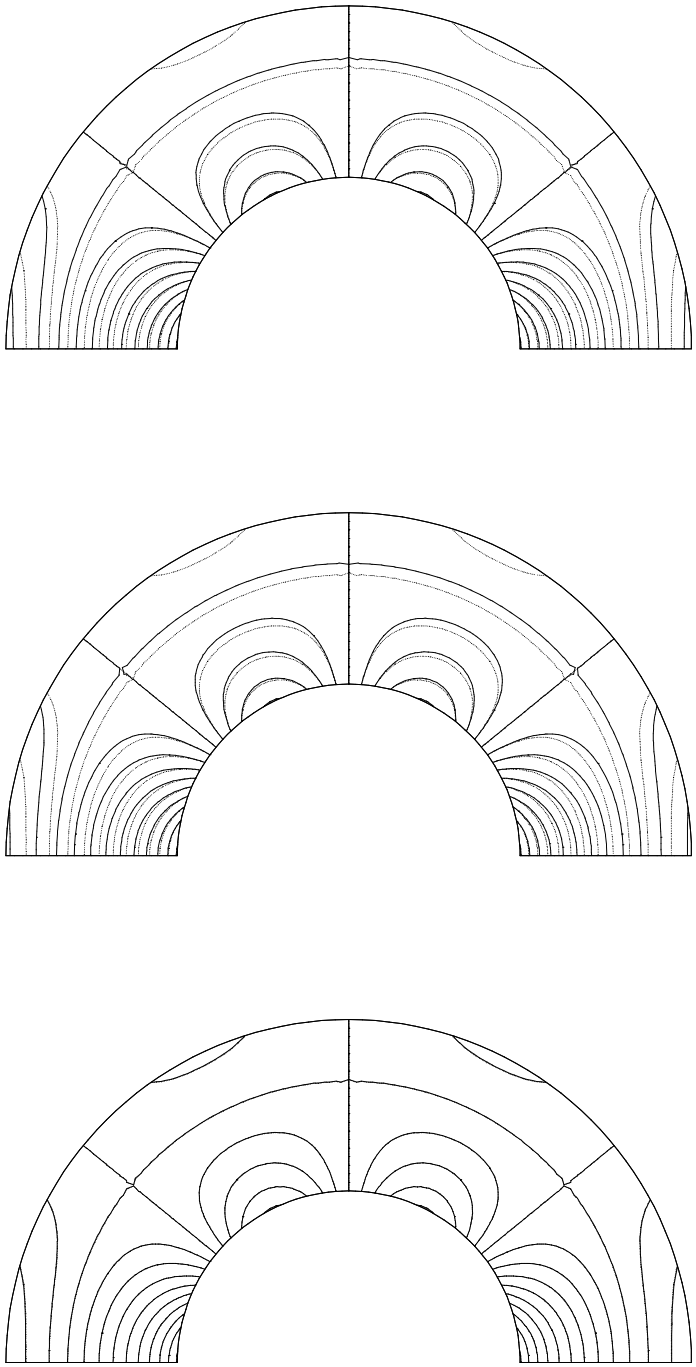

Figure 5.13: Radiation from sphere with polar harmonic $n = 3$ and normalized frequency $ka = 3$. Contours of space-time solution at $t = 20$ using local boundary conditions, (Top): 'plane-wave' S_0, (Middle): first-order S_1, (Bottom): second-order S_2. (dotted contours denote analytical solution).

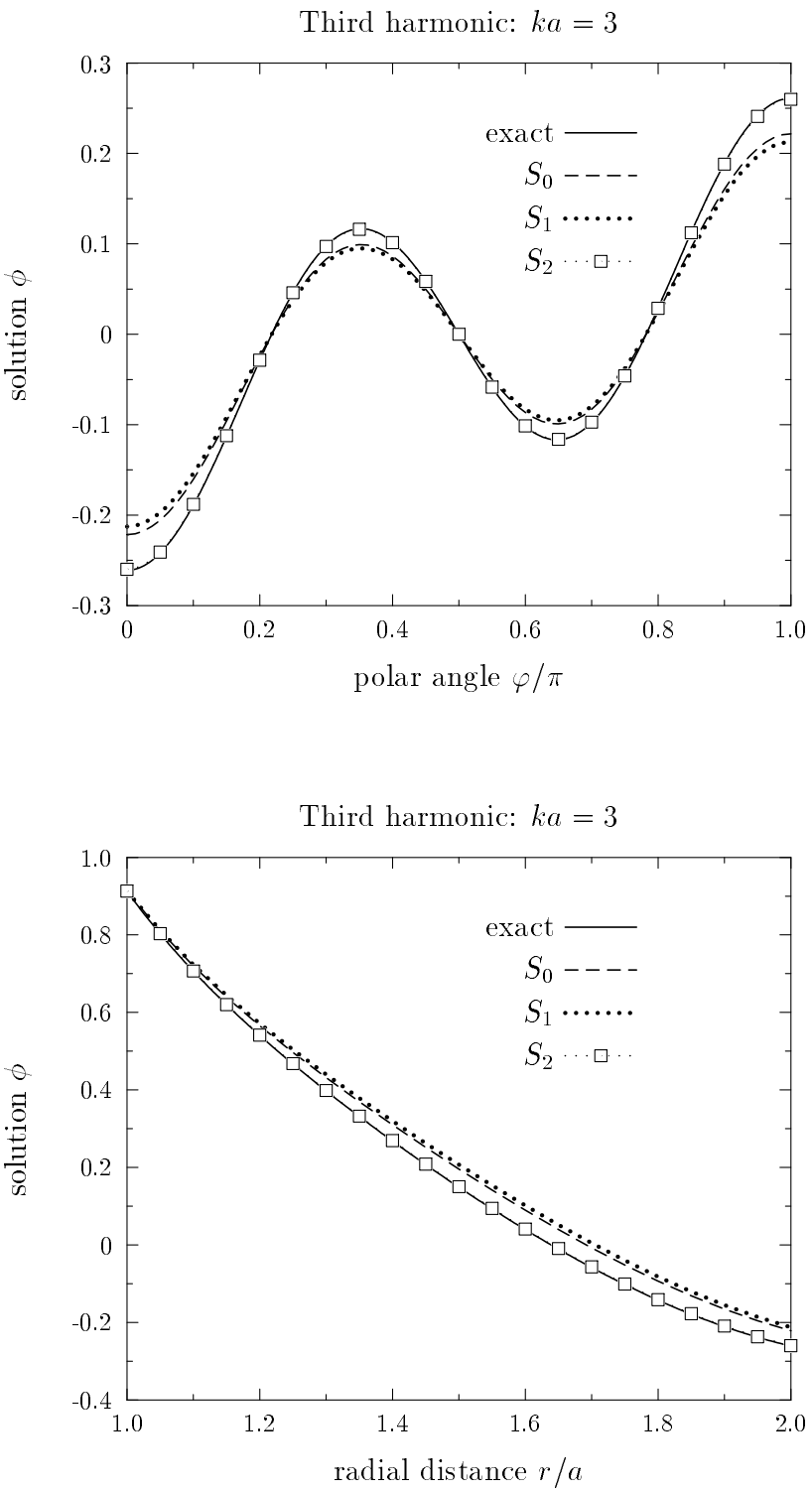

Figure 5.14: Spherical wave harmonic $n = 3$: Results at $t = 20$, comparing the 'plane-wave' S_0, first-order S_1, and second-order S_2 boundary conditions. (Top): Solution profile on the artificial boundary $r = R$. (Bottom): Solution plotted along radial line at $\varphi = 0$.

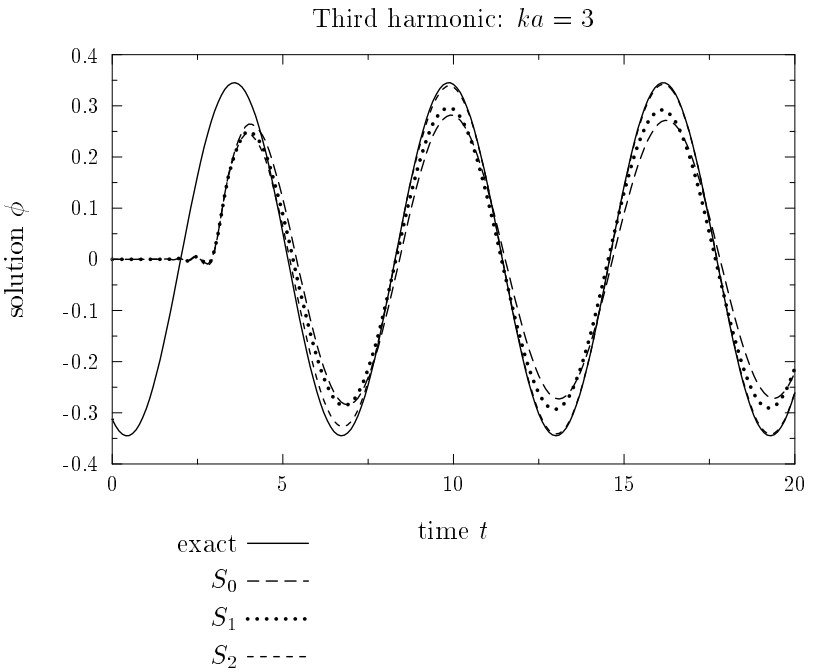

Figure 5.15: Time-dependent solution at a point on the artificial boundary, i.e. $r = R$ and $\varphi = 0$. Results show the transient solution as it is driven to steady-state.

comparison, the solution using $\mathbb{S}_2$ is remarkably accurate; with the numerical and analytical solutions almost indistinguishable.

This example demonstrates an important property of the approximate local boundary conditions: *As the frequency, normalized with respect to the characteristic dimension of the problem increases, the local boundary conditions become increasingly accurate.*

Harmonic $n = 4$:

Figures 5.16 through 5.18 show the solution for the polar harmonic $n = 4$ with a non-dimensional wavenumber $ka = 3$ at time $t = 15$. For this loading, the $\mathbb{S}_2$ local operator is able to maintain an accurate solution, while the solution using the low-order operators $\mathbb{S}_0$ and $\mathbb{S}_1$ have deteriorated significantly. When the harmonic loading is raised to $n = 5$, all three boundary operators tested exhibit large errors in the solution (not shown). In order to obtain accurate solutions for this loading and frequency, the artificial boundary must be moved further away from the sphere, requiring a larger domain, and an increase in computational expense.

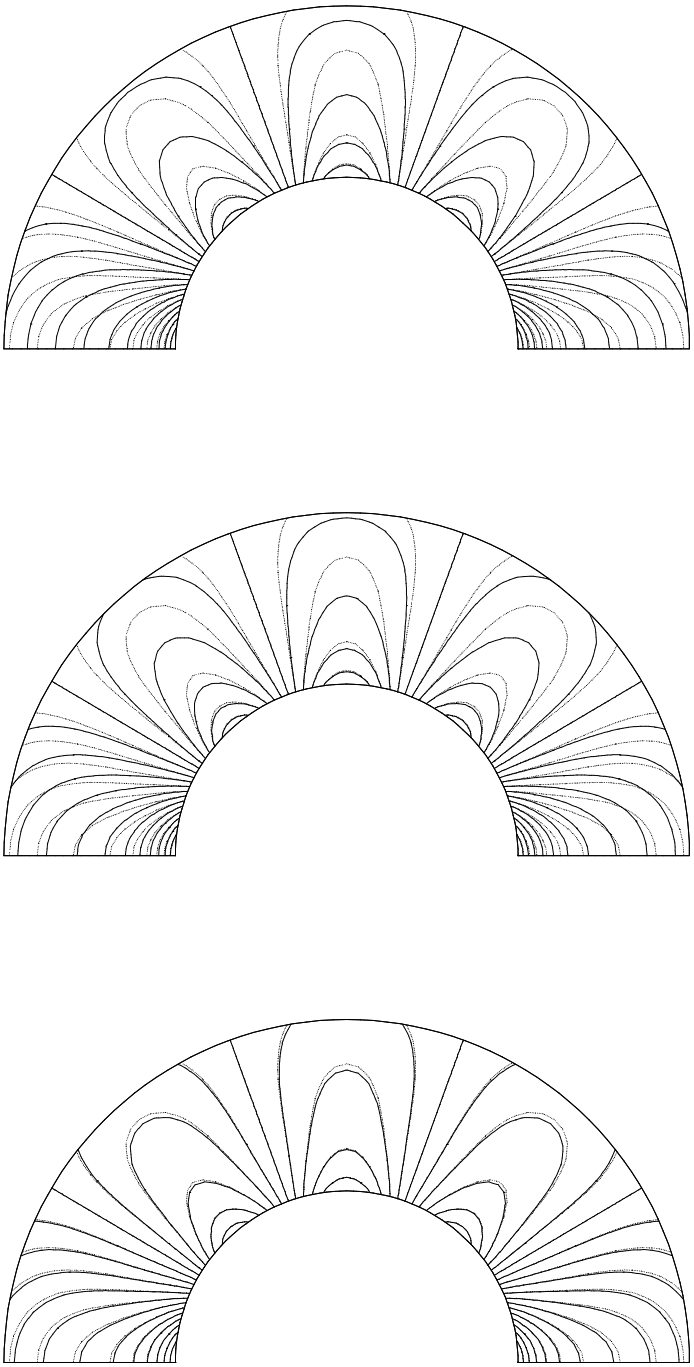

Figure 5.16: Radiation from sphere with polar harmonic $n = 4$ and normalized frequency $ka = 3$. Contours of space-time solution using local boundary conditions, (Top): 'plane-wave' S_0, (Middle): first-order S_1, (Bottom): second-order S_2. (dotted contours denote analytical solution).

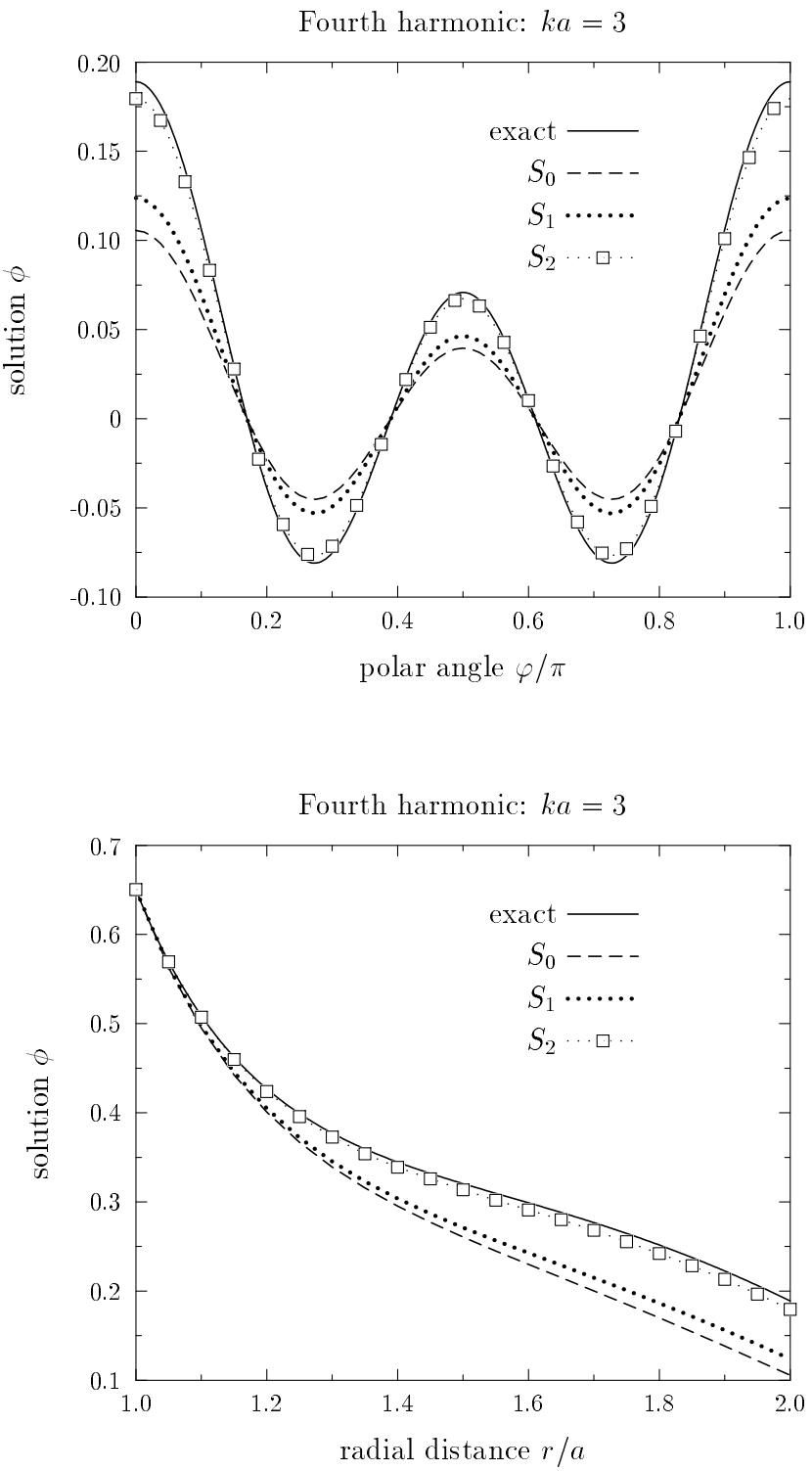

Figure 5.17: Spherical wave harmonic $n = 4$: Results comparing the 'plane-wave' S_0, first-order S_1, and second-order S_2 boundary conditions. (Top): Solution profile on the artificial boundary $r = R$. (Bottom): Solution plotted along radial line at $\varphi = 0$.

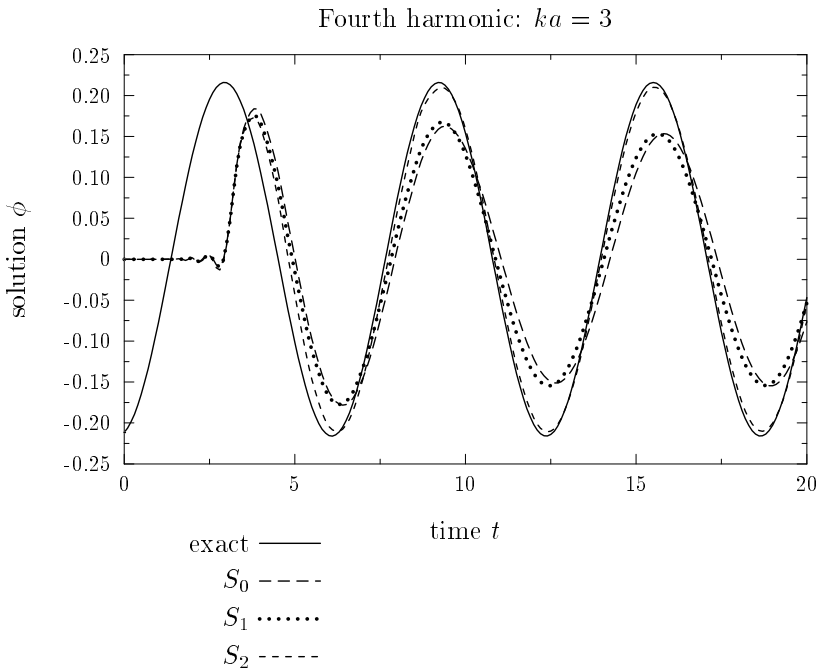

Figure 5.18: Time-dependent solution at a point on the artificial boundary, i.e. $r = R$ and $\varphi = 0$. Results show the transient solution as it is driven to steady-state.

5.3.2 Radiation from a circular piston on a sphere

To study a more complicated problem involving an infinite number of spherical wave harmonics, consider the non-uniform radiation from a circular piston subtending a polar angle $0 \leq \varphi \leq \varphi_p = 13.5^o$ on a submerged sphere of radius $r = a$. The piston has a constant inhomogeneous value $\phi(a,t) = \sin\omega t$ for $t > 0$. Elsewhere on the wet surface, the solution vanishes. The steady-state analytical solution for the velocity potential is,

$$\phi(r,\varphi,t) = -\frac{1}{2}\mathrm{Imag}\left\{\sum_{n=0}^{\infty}\frac{h_n(kr)}{h_n(ka)}\left[P_{n-1}(\cos\varphi_p) - P_{n+1}(\cos\varphi_p)\right]P_n(\cos\varphi)\mathrm{e}^{-i\omega t}\right\} \tag{5.55}$$

This problem gives rise to the interesting feature that as the wave generated at the piston pole $\varphi = 0^o$, travels along longitudes, it is attenuated by a geometrical spreading loss. As the diameter of the sphere increases when compared to a wavelength, the wave field departs more and more from a point source pattern, and in the region opposite the piston pole $\varphi = 180^o$, the amplitude is significantly lower.

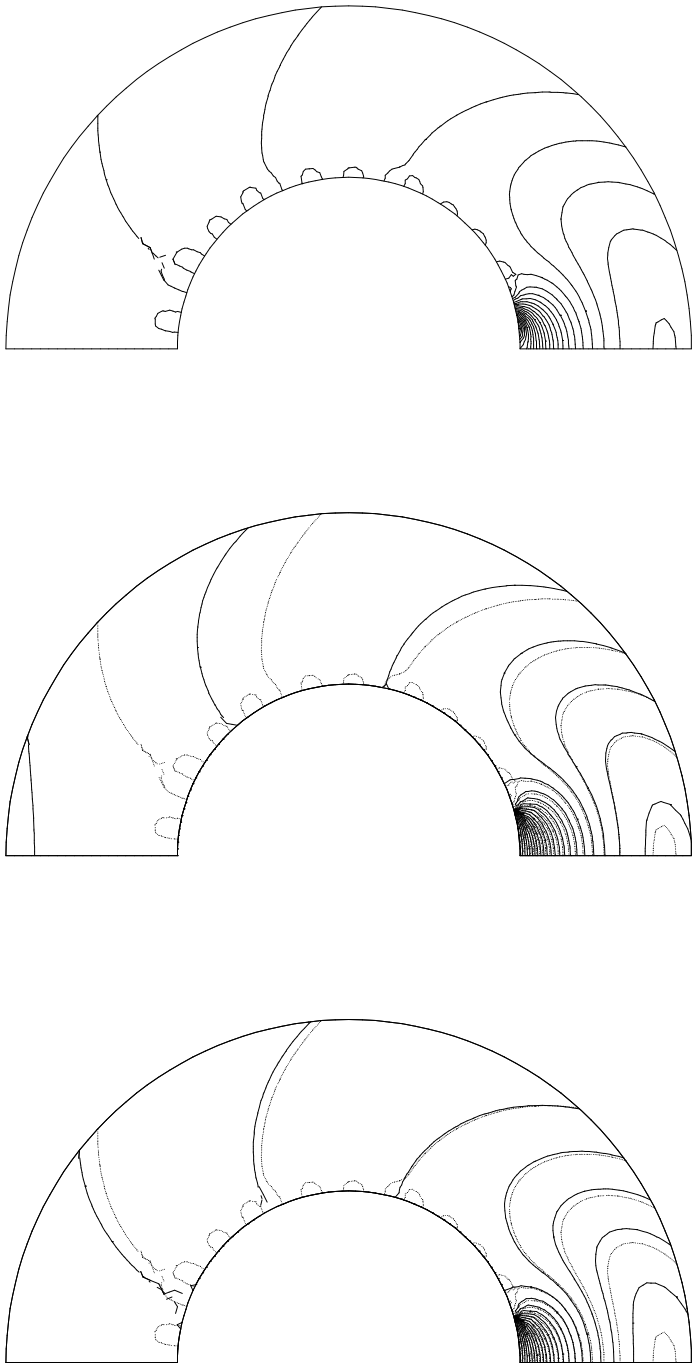

Figure 5.19: Solution contours for radiating piston on a sphere: (Top): Analytic series solution at time $t = 30$ and $ka = 3$. (Middle): Space-time solution with S_1 local boundary condition. (Bottom): Space-time solution with S_2 local boundary condition. (dotted contours denote exact solution)

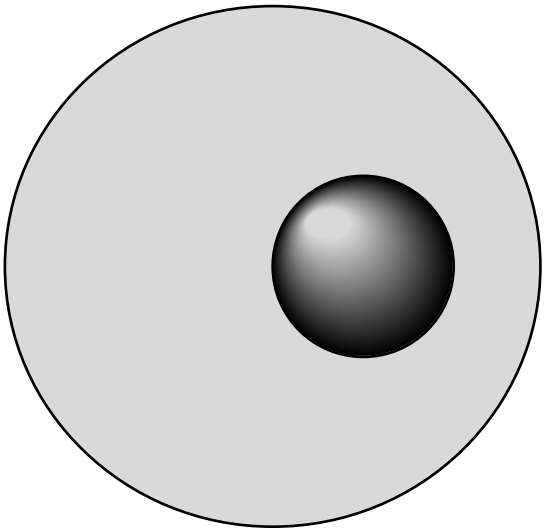

Figure 5.20: Illustration of a spherical radiator of radius a, offset from the center of a spherical artificial boundary of radius $3a$.

In this example, the properties and discretization are unchanged from the previous problem considered. Figure 5.19 (top) shows the contours of the analytical series solution, nodally interpolated with the mesh employed. The low-amplitude oscillations in the vicinity of the wet surface are a product of the difficulty the series solution has in resolving the discontinuity in the loading condition at $\varphi_p = 13.5^o$, and are not relevant to the validation of the numerical results. In Figure 5.19 (middle) and (bottom), results for the space-time solution show a significant improvement in the solution using $\mathbb{S}_2$, in comparison to the solution using $\mathbb{S}_1$. Near the piston pole, both solutions accurately capture the physics of the problem, but as the wave pattern spreads to the backside, the solution using $\mathbb{S}_1$ deteriorates significantly while $\mathbb{S}_2$ maintains an accurate solution throughout the entire computational domain.

5.3.3 Nonconcentric spherical radiator

As the final example in this chapter, consider a sphere of radius $r = a$, pulsating with a uniform sine pulse, $\phi(a,t) = \sin \omega t$ and $\omega = \pi$, during the short time interval $t \in [0,1]$. Initial conditions are set to zero and the wave speed is $c = 1$. The exact solution to this problem is an outgoing spherical wave of short duration with a $1/r$

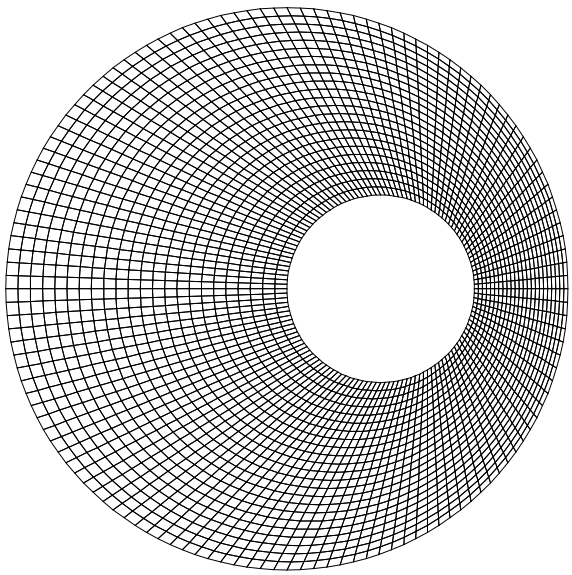

Figure 5.21: Computational domain for a sphere shifted from the center of a spherical non-reflecting boundary. Spatial discretization: Upper half modeled with 1518 axisymmetric elements using quadratic interpolation.

amplitude decay:

$$\phi(r\,,\,t) \quad = \quad \left(\frac{a}{r}\right)\sin\omega(t-\bar{r}/c) \tag{5.56}$$

where $\bar{r} = r - a$ is the radial distance from the spherical radiator and $(t - \bar{r}/c) \in [0, 1]$.

If the radiating sphere is placed concentric with a spherical artificial boundary, as was done in the previous examples of this chapter, then for the uniform radiation field given in (5.56), the problem is trivial in that the first order $\mathbb{S}_1$, and higher order local non-reflecting boundary conditions are all exact. In order to obtain a challenging problem, the radiating sphere is shifted from the center of the spherical artificial boundary Γ_∞, to a nonconcentric position. In this example, the radiating sphere is offset by a distance a, with the radius of Γ_∞ set at $R = 3a$, see Figure 5.20. With this positioning, wave fronts traveling outward along radial lines will strike the artificial boundary at oblique angles. The closer the radiating sphere gets to the edge of Γ_∞, the more acute this angle becomes, making it increasingly difficult for the approximate local boundary conditions to transmit outgoing waves without spurious reflection.

Figure 5.21 shows the computational domain discretized with 1518 axisymmetric elements using quadratic interpolation. Figure 5.22 shows the elevated contours of the time-discontinuous Galerkin solution using the second-order local boundary operator $\mathbb{S}_2$ applied to Γ_∞. In the upper left corner of Figure 5.22, the solution is shown at the end of the initial sine pulse at time $t = 1$. As time progresses, the initial pulse propagates outward from the sphere as a uniform spherical wave pulse of decreasing amplitude. The scales used in the illustrations are normalized at each time step to enhance the visibility of the solution features. After $t = 1$, the spherical pulse begins to pass through the artificial boundary Γ_∞ with negligible reflection. At time $t = 3.5$, as the pulse is just leaving the computational domain, it is noted that the numerical solution displays only insignificant traces of low amplitude reflected waves behind the outgoing wave front. For time steps beyond $t = 4$ (not shown), the low amplitude reflected waves are several orders of magnitude smaller than the amplitude of the physical wave, and are quickly damped out by the numerical dissipation inherent in the time discontinuous Galerkin method. This result illustrates the remarkable performance of the second-order operator $\mathbb{S}_2$ to transmit waves striking the artificial boundary at rather severe angles.

For comparison, this same problem was solved with the low-order boundary operator $\mathbb{S}_1$. Figures 5.23 and 5.24 show the elevated contours at times $t = 2.0$ and $t = 2.5$ respectively, comparing the solution using either $\mathbb{S}_1$ or $\mathbb{S}_2$. The solution using $\mathbb{S}_1$ exhibits significant reflections as the outgoing pulse passes through Γ_∞, as indicated by the elevated contours on the front (right) side of the sphere. In comparison, the solution using $\mathbb{S}_2$ shows no observable reflections from Γ_∞. This conclusion is summarized in Figure 5.25 as a plot of the solution on the artificial boundary Γ_∞ at the axis of symmetry, $\varphi = 0$. The solution using $\mathbb{S}_2$ shows the correct amplitude and phase for the outgoing pulse, and shows no observable reflections behind the wave front. In contrast, the solution using $\mathbb{S}_1$ shows an increase in the maximum amplitude of the outgoing pulse as well as significant reflections, as manifested by the non-zero amplitudes appearing for times $t > 2$.

5.4 Summary and Conclusions

When domain based computational methods are used to model the exterior fluid/structure interaction problem, accurate non-reflecting boundary conditions are required on the artificial truncation boundary. If the form of the non-reflecting boundary condition is over-simplified, for example the simple PW-damper defined in (2.24), spurious reflected waves can be generated at the artificial boundary, which can substantially degrade the accuracy of the numerical solution. In order to minimize the effect of spurious reflections, the computational region can be enlarged so that the artificial boundary is far from the radiator/scatterer, however, this will require an increase in the number of solution variables, with a subsequent increase in computational expense. It is thus preferable to use on Γ_∞ a non-reflecting boundary condition that is sufficiently accurate even when the artificial boundary Γ_∞ is very close to the radiating structure.

In this chapter, new local time-dependent non-reflecting boundary conditions which are exact for the first N spherical wave harmonics have been developed for the three-dimensional wave equation. The development of these boundary conditions begins from the truncated Dirichlet-to-Neumann (DtN) map in the frequency domain. By applying an inverse Fourier transform to the localized form of the DtN map, local time-dependent boundary conditions are obtained. We showed how these local boundary conditions can easily be incorporated into the time-discontinuous variational formulation as natural boundary conditions in both space and time, preserving the banded, sparse date structure of the method.

In addition, we demonstrated that an exact local in time counterpart exists for the spatially nonlocal and frequency dependent DtN non-reflecting boundary condition. This resulted in a sequence of exact boundary conditions that are nonlocal in space yet retain their locality in time. This new sequence of local in time and nonlocal in space nonreflecting boundary conditions allows for the use of C^0 interpolations in both the time and space dimensions. As a result, when implemented in the time-discontinuous finite element formulation, this sequence appears to offer the greatest potential for the implementation of accurate boundary operators beyond second-order.

A favorable feature inherited by the non-reflecting boundary conditions proposed

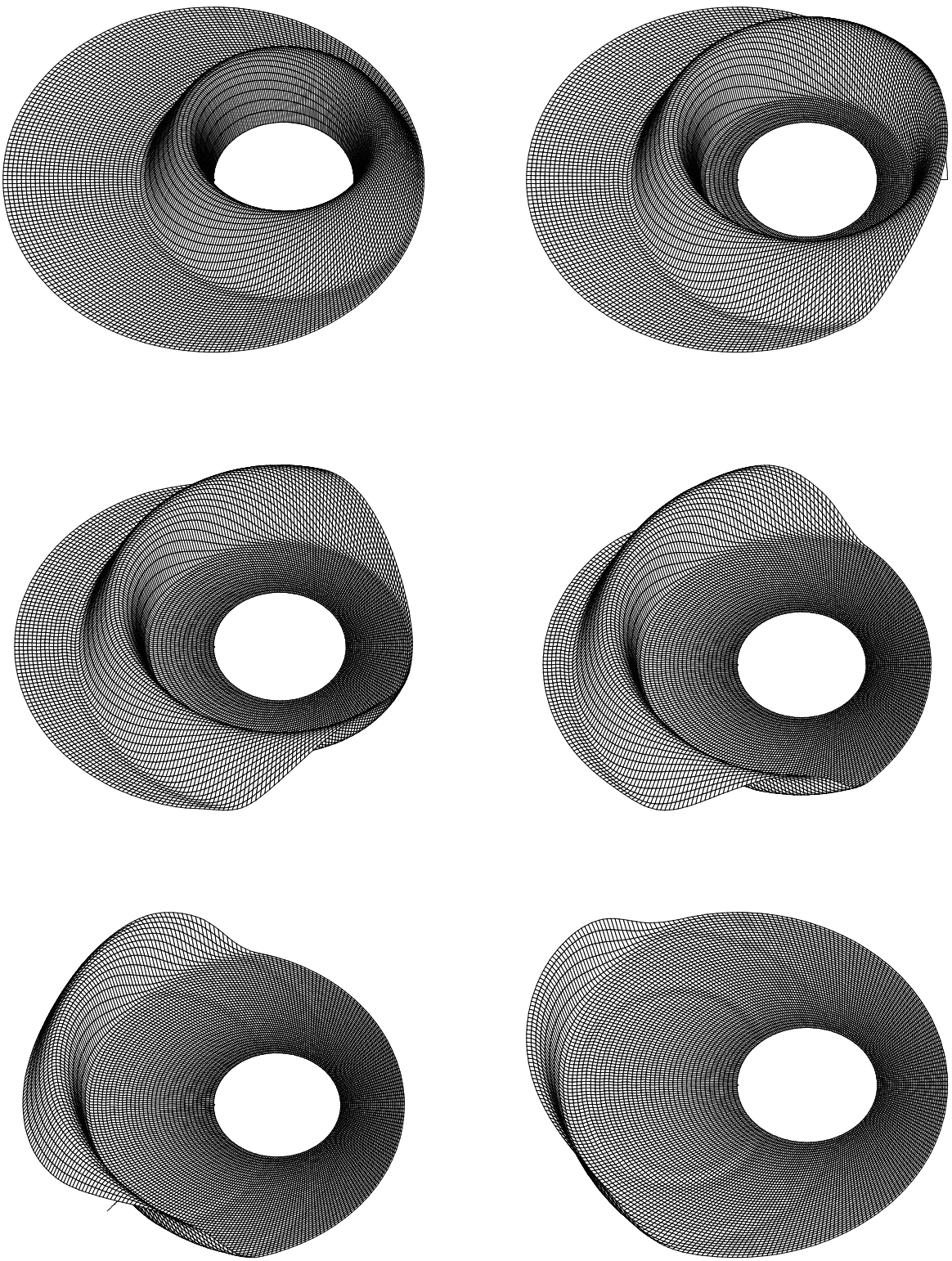

Figure 5.22: Radiation from a nonconcentric sphere. Elevated solution contours shown at the end of the initial pulse at $t = 1$ and later times $t = 1.5$ through $t = 3.5$ in increments of $\Delta t = 0.5$.

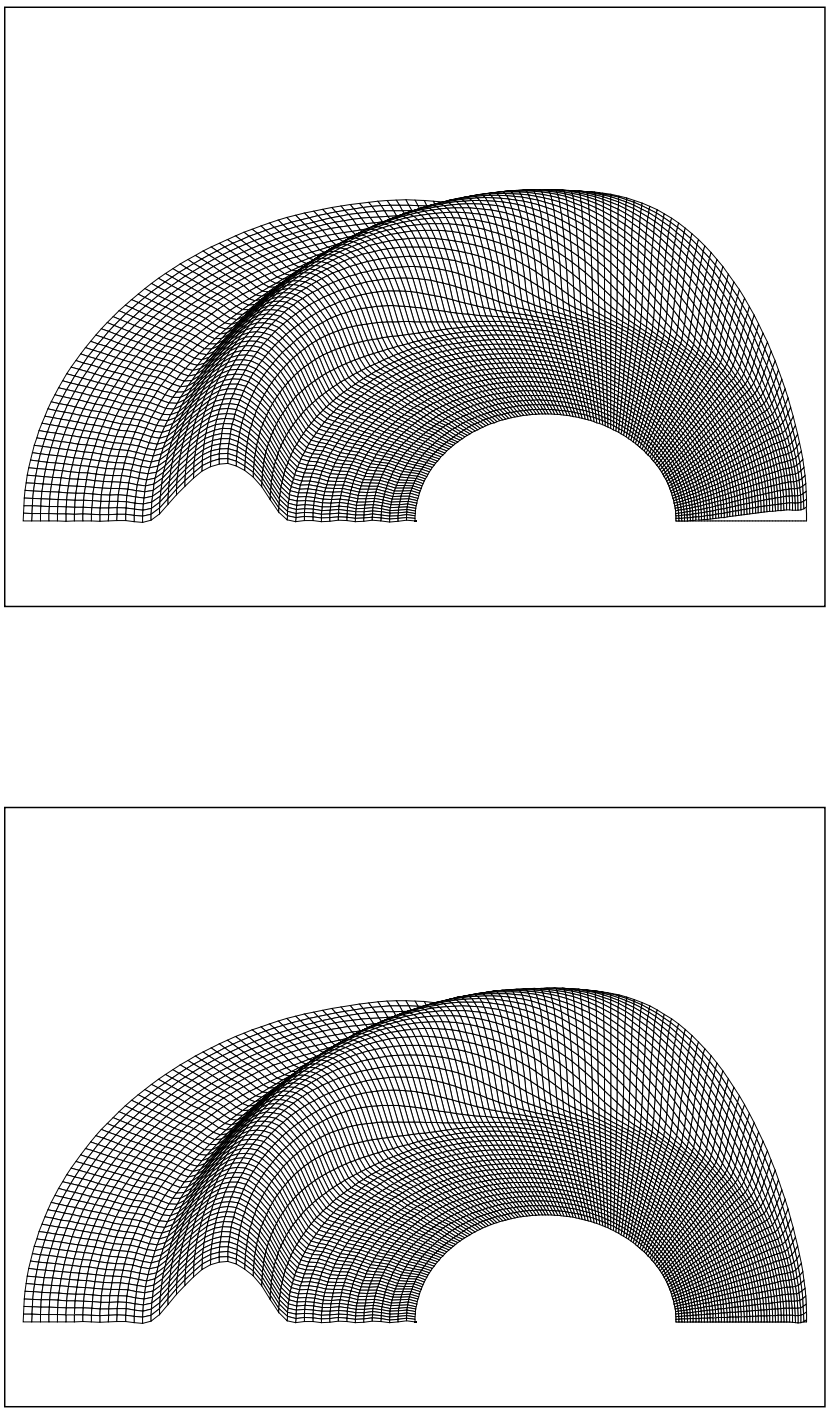

Figure 5.23: Radiation from a nonconcentric sphere. Elevated contours shown at $t = 2.0$. Space-time solution using (top) $\mathbb{S}_1$ local boundary condition. (bottom) $\mathbb{S}_2$ local boundary condition.

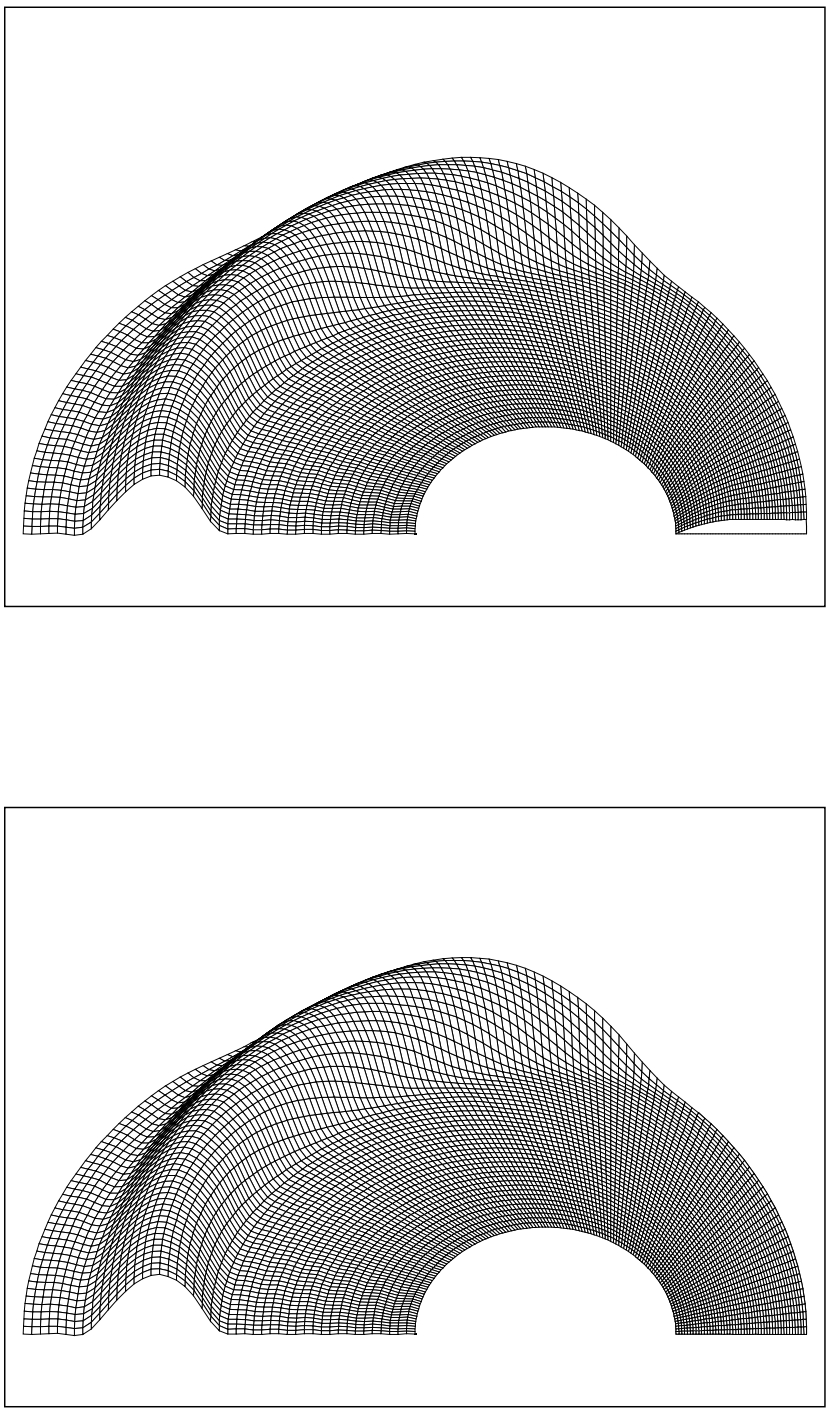

Figure 5.24: Radiation from a nonconcentric sphere. Elevated contours shown at $t = 2.5$. Space-time solution using (top) $\mathbb{S}_1$ local boundary condition. (bottom) $\mathbb{S}_2$ local boundary condition.

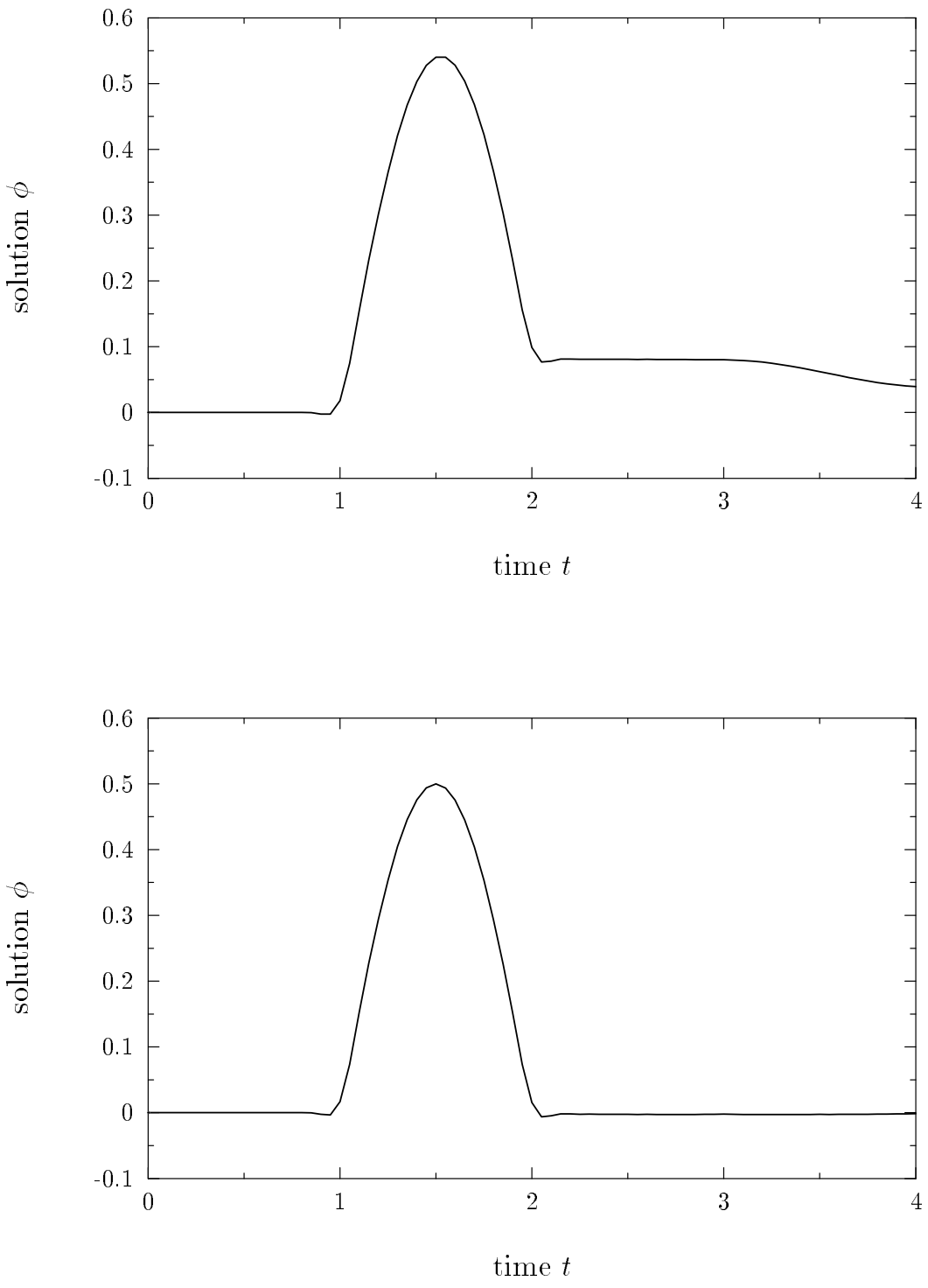

Figure 5.25: Radiation from a nonconcentric sphere: Solution on the artificial boundary Γ_∞, at the axis of symmetry $\varphi = 0$. (top) $\mathbb{S}_1$ local boundary condition. (bottom) $\mathbb{S}_2$ local boundary condition.

in this chapter is that they exactly represent the solution as a series of outgoing spherical wave harmonics. This property plays an important role in the understanding of how individual wave harmonics contribute to the accuracy and stability of the solution as effected by the radial distance of the artificial boundary from the source, and the geometric complexity and frequency content of the outgoing waves. In contrast, a physical understanding of the harmonic contribution to the accuracy and stability of boundary operators based on power series (multipole) expansions, such as the sequence derived by Bayliss and Turkel, is currently lacking.

Numerical solutions for some canonical time-dependent acoustic radiation problems demonstrated the improved accuracy that results from the use of the high-order non-reflecting boundary conditions within the space-time finite element method. In particular, the effects of increasing spherical harmonics n, frequency $\omega = kc$, and the position of the truncation boundary R, on the accuracy of the space-time finite element solution using the local radiation boundary operators was investigated. Results from this study are summarized in the following:

1. The local boundary operators provide increasing accuracy with the order N used in the truncated DtN series.

2. The accuracy depends strongly on the normalized frequency ka, in that the local operators can accurately capture increased wave harmonics as the frequency (wavenumber) is increased relative to the dimension of the radiator/scatterer.

3. The operators are increasingly accurate as the position R of the artificial boundary is moved further away from the radiator/scatterer.

Results from these studies, together with the numerical results obtained from a vibrating piston on a spherical baffle, and the transient radiation from a non-concentric sphere, support the conclusion that the local second-order non-reflecting boundary condition $\mathbb{S}_2$ exhibits superior accuracy when compared to the low-order local boundary conditions $\mathbb{S}_0$ and $\mathbb{S}_1$, with no additional cost. In addition, it has been demonstrated that when implemented in the time-discontinuous Galerkin method, the second-order operator $\mathbb{S}_2$ provides sufficient accuracy for the problems tested. These results suggests that when used with the proper consideration given to the position of the non-reflecting boundary, and the frequency content of the solution, then the local

second-order operator provides an economical means to achieve accurate solutions to the transient structural acoustics problem in exterior domains. It remains to be seen what (if any) additional advantage in terms of accuracy and economy can be achieved by the implementation of the third-order operators derived in this chapter.